



RESEARCH ARTICLE

10.1029/2019JB017464

Key Points:

- Creep of quartz sand by subcritical cracking is strongly impacted by pore fluid chemistry
- Low water content and low fluid pH inhibit crack tip bond hydrolysis and hence creep
- Injected fluid chemistry may influence reservoir compaction and induced seismicity

Correspondence to:

M. T. W. Schimmel,
m.t.w.schimmel@uu.nl

Citation:

Schimmel, M. T. W., Hangx, S. J. T., & Spiers, C. J. (2019). Impact of chemical environment on compaction creep of quartz sand and possible geomechanical applications. *Journal of Geophysical Research: Solid Earth*, 124, 5584–5606. <https://doi.org/10.1029/2019JB017464>

Received 2 FEB 2019

Accepted 25 MAY 2019

Accepted article online 4 JUN 2019

Published online 23 JUN 2019

Impact of Chemical Environment on Compaction Creep of Quartz Sand and Possible Geomechanical Applications

M. T. W. Schimmel¹ , S. J. T. Hangx¹ , and C. J. Spiers¹

¹HPT Laboratory, Department of Earth Sciences, Faculty of Geosciences, Utrecht University, Utrecht, the Netherlands

Abstract Induced seismicity and surface subsidence are adverse effects of natural gas and geothermal energy production that may present barriers to their use as low-carbon alternatives to coal and oil. The driving force for these unwanted effects is compaction of the reservoir, which can potentially be mitigated by injecting (pressurized) fluids that restore the pore pressure and chemically inhibit compaction. We conducted uniaxial compaction experiments on quartz sand aggregates to investigate the effect of pore fluid chemistry on time-dependent compaction (creep). In addition to a low-vacuum (dry) environment, supercritical fluids (N₂, CO₂, and wet CO₂), simple aqueous solutions (three HCl solutions and a NaOH solution), and complex aqueous solutions with additives (AlCl₃, AMP, and washing detergent) were employed. N₂, CO₂, and fluids containing scaling inhibitor (AMP), as well as wastewater (detergent solution) are generally considered for injection. Compaction creep was enhanced in fluid-saturated environments compared to dry. Wet CO₂ caused more creep with faster strain rates than the relatively dry CO₂ and N₂ environments. Experiments conducted with simple aqueous solutions exhibited a clear pH dependency. The complex aqueous solutions enhanced creep compared to their simple solution counterpart with similar pH. Based on acoustic emission data and microstructural analyses, we inferred that compaction creep was controlled by subcritical crack growth, aided by water, hydroxyl ions, and additives. If microcracking also controls compaction in reservoir sandstones, these results indicate that injection of supercritical fluids or acidic solutions may mitigate reservoir compaction.

1. Introduction

In the drive to reduce carbon emissions, natural gas can play an important interim role as a lower carbon alternative to coal and oil (IEA, 2016). However, adverse effects of prolonged production, such as induced seismicity and surface subsidence, are becoming apparent in gas fields worldwide. These effects have been observed above many sand and sandstone reservoirs (Suckale, 2010). Examples include a number of onshore gas fields in the Netherlands, for example, the Annerveen, Eleveld, and Roswinkel fields (Van Eck et al., 2006; Van Eijs et al., 2006), as well as fields in the Gulf of Mexico (Ostermeier, 1995), the Gazli field in Uzbekistan (Simpson & Leith, 1985), the Ravenna Terra field in Italy (Menin et al., 2008), the Rotenburg field in Germany (Dahm et al., 2007), and the Saxet field in Texas, USA (Suckale, 2010). Induced seismicity and surface subsidence can cause significant surface damage and environmental impact (Gambolati & Teatini, 2015; Suckale, 2009). In turn, the associated risks, and public perception thereof, may reduce the potential for natural gas to contribute to the energy transition.

In the case of gas fields, induced seismicity and surface subsidence are the result of production-induced pore pressure depletion, causing compaction at the reservoir level (Spiers et al., 2017). Upon production, the pore pressure (P_p) in the reservoir decreases relative to the overburden stress (σ_v), which increases the vertical effective stress ($\sigma_{v,eff} = \sigma_v - P_p$) acting on the load-bearing structure of the reservoir rock. This leads to recoverable poroelastic and, in some cases, permanent, inelastic compaction of the reservoir rock (Bernabé et al., 1994; Pijenburg et al., 2018; Shalev et al., 2014), potentially with a time- (creep) or rate-dependent component (Doornhof et al., 2006; Nagel, 2001). Permanent compaction occurs when the effective stress acting on the rock becomes large enough to activate inelastic grain-scale deformation processes, such as grain rearrangement (Menéndez et al., 1996), grain and grain contact failure by equilibrium or subcritical crack growth (Brantut et al., 2012; Brzesowsky, Hangx, et al., 2014; Brzesowsky, Spiers, et al., 2014), intergranular clay film deformation (Spiers et al., 2017), pressure solution (Dewers & Hajash, 1995; Gratier et al., 2009; Schutjens,

©2019. The Authors.

This is an open access article under the terms of the Creative Commons Attribution-NonCommercial-NoDerivs License, which permits use and distribution in any medium, provided the original work is properly cited, the use is non-commercial and no modifications or adaptations are made.

1991; Spiers et al., 2004), and intergranular frictional slip (Spiers et al., 2017). While poroelastic deformation is recoverable and relatively easy predicted (Wang, 2000), permanent deformation and particularly creep are not making long-term predictions of compaction uncertain (Mossop, 2012) and evaluation of associated seismic hazards difficult.

In the Netherlands, the occurrence of production-induced seismicity and surface subsidence has led to plans to abandon the giant Groningen gas field by 2030 (Van Thienen-Visser & Breunese, 2015; Wiebes, 2018a). However, to aid the energy transition and maintain natural gas supply, production from small onshore and offshore gas fields will continue (Wiebes, 2018b). Here and in other gas fields around the world, this raises the question of whether options exist for mitigating adverse reservoir compaction, subsidence, and seismic effects.

One strategy for mitigating reservoir compaction is waterflooding, that is, water injection into a reservoir to restore and maintain the pore pressure at the initial level. This was successfully applied in the Wilmington field in California, USA, for example, producing an elastic reservoir and surface rebound of approximately 30 cm (Colazas & Strehle, 1995). Though fluid injection may introduce new risks (Schimmel et al., 2019), it can, in principle, be applied to restore the reservoir pore pressure, lowering the effective overburden stress acting on the reservoir and removing much of the mechanical driving force for compaction. Potential fluids for pressure restoration are (waste)water, CO₂, and N₂ (Bachu & Gunter, 2005; Suckale, 2009). Additionally, permanent compaction can potentially be mitigated by regulating the chemical environment, such that chemically coupled grain-scale deformation processes are inhibited. For example, while compaction creep of quartz sand via subcritical crack growth and grain failure is known to be enhanced by highly alkaline fluids (Hangx et al., 2010) and fluids containing Na⁺ ions (Brzesowsky, Hangx, et al., 2014), it is inhibited by acidic fluids (Hangx et al., 2010). Similar fluid compositional effects, influencing the rate of stress-driven dissolution and precipitation processes (e.g., pressure solution), have also been observed (Dove, 1999; Dove & Crerar, 1990; Dove & Nix, 1997; Iler, 1973). It is the rate at which these grain-scale processes operate that controls the timescale at which compaction creep occurs. Since subcritical cracking, dissolution-precipitation processes, clay sorption, and ion-exchange processes are all controlled by interactions with pore fluid species at the atomic scale, the possibility exists, at least in theory, that reservoir compaction, subsidence, and associated seismicity can be influenced by changing pore fluid chemistry through the injection of mitigation agents.

We studied the effect of pore fluid chemistry on compaction creep in quartz sand aggregates, as an analogue for clean, highly porous, quartz-rich reservoir sands and sandstone. Creep is specifically addressed, because it is not yet well understood and can potentially cause reservoir compaction even after production has ceased (Mossop, 2012). Going beyond previous work, we focused on fluids typically considered for pressure maintenance or for permanent storage, for example, water, wastewater, CO₂, and N₂ (Bachu & Gunter, 2005; Suckale, 2009), as well as agents, such as AlCl₃, a quartz dissolution inhibitor (Iler, 1973), and scaling inhibitors used in water treatment facilities (Knepper, 2003) and geothermal energy production (Finster et al., 2015). Uniaxial (oedometer) compaction experiments were performed on cylindrical sand samples at constant effective stress (35 MPa) and constant temperature (80 °C), simulating typical reservoir depths of 2–4 km. Insight into the deformation mechanisms operating at the grain scale was obtained via acoustic emission (AE) counting and by means of microstructural study and grain size analysis applied before and after individual compaction tests. The tests revealed that compaction creep in our granular quartz samples was controlled by subcritical microcracking, a process strongly influenced by pore fluid chemistry. More specifically, water content and pore fluid pH were inferred to control the amount and rate of compaction creep.

2. Experimental Method

2.1. Sample Material and Pore Fluid Preparation

In this study, we used sand taken from the Heksenberg Formation, exposed in the Beaujean Quarry, Heerlen, the Netherlands. Sample material was prepared as described in previous work (Brzesowsky et al., 2011; Brzesowsky, Hangx, et al., 2014; Brzesowsky, Spiers, et al., 2014). The sand was sieved to obtain a grain size fraction of $196 \pm 16 \mu\text{m}$. X-ray diffraction analysis and inductively coupled plasma emission spectroscopy measurements on the sieved material indicated a quartz content of >99 wt% with zircon and Na-rich feldspar present as principal trace minerals. The feldspar mineral was successfully removed by

Table 1

Overview of Complete Set of Uniaxial Compaction Creep Experiments Performed on Quartz Sand Aggregates in This Study

Experiment	φ_c (%)	Chemical environment	Fluid pH	Duration creep phase (hr)	φ_f (%)	ε_f (%)	TS or GS analysis	Crack densities ($P_L^ /P_L^\perp$; mm ⁻¹)
Control experiments								
dry-09	38.4	Low vacuum (dry)	—	19	38.3	0.2	GS	—
dry-10	39.7	Low vacuum (dry)	—	66	39.4	0.4	—	—
dry-11 ^a	39.0	Low vacuum (dry)	—	21	38.7	0.5	TS	1.3/1.1
Supercritical fluids ($P_p = 10$ MPa)								
N2-01	38.9	N ₂	—	19	38.3	0.9	TS	1.3/1.2
N2-02 ^a	38.8	N ₂	—	40	38.2	0.9	GS	-
CO2-01 ^a	38.7	CO ₂	—	15	38.0	1.1	GS	-
CO2-02	39.1	CO ₂	—	18	38.3	1.3	TS	1.2/1.1
CO2-03	38.5	CO ₂	—	88	37.4	1.8	—	—
wCO2-03	38.9	Wet CO ₂	—	24	37.8	1.8	GS	—
wCO2-04	39.0	Wet CO ₂	—	71	37.6	2.2	—	3.0/2.3
wCO2-05 ^a	38.7	wet CO ₂	—	18	37.8	1.5	TS	2.1/2.0
Simple aqueous solutions (atmospheric pore pressure)								
1pH-01	39.2	HCl solution	1	20	38.2	1.6	GS	—
1pH-02	38.4	HCl solution	1	41	37.6	1.3	—	—
1pH-03	39.0	HCl solution	1	17	38.1	1.5	—	—
1pH-04 ^a	38.9	HCl solution	1	19	37.9	1.6	TS	1.7/1.3
2.4pH-01	38.0	HCl solution	2.4	17	37.2	1.3	GS	—
2.4pH-02 ^a	38.7	HCl solution	2.4	31	37.5	1.8	—	—
2.4pH-03	38.6	HCl solution	2.4	18	37.7	1.4	TS	1.3/0.8
4pH-01	38.7	HCl solution	4	18	37.5	2.0	TS	1.7/1.4
4pH-02	38.6	HCl solution	4	18	37.4	1.9	GS	—
4pH-03 ^a	38.7	HCl solution	4	91	37.1	2.6	—	—
DI-08	38.8	Distilled water	5.9	18	37.4	2.2	—	—
DI-09 ^a	38.7	Distilled water	5.9	17	37.4	2.1	TS	3.4/2.4
DI-10	38.5	Distilled water	5.9	18	37.3	1.8	GS	—
DI-11	38.9	Distilled water	5.9	63	37.2	2.8	—	—
9pH-01	38.6	NaOH solution	9	22	37.0	2.6	GS	—
9pH-02	38.5	NaOH solution	9	20	36.9	2.5	TS	3.4/3.4
9pH-03 ^a	38.9	NaOH solution	9	66	36.7	3.3	—	—
Complex aqueous solutions (atmospheric pore pressure)								
AMP-01	39.0	AMP solution	2.5	16	37.8	1.8	—	—
AMP-02	39.0	AMP solution	2.5	19	37.9	1.8	GS	—
AMP-03 ^a	38.7	AMP solution	2.5	19	37.7	1.7	TS	2.5/2.4
AMP-04	38.8	AMP solution	2.5	42	37.5	2.0	—	—
AlCl3-01 ^a	38.8	AlCl ₃ solution	3.5	19	37.6	1.9	TS	1.9/1.6
AlCl3-02	38.8	AlCl ₃ solution	3.5	22	37.8	1.6	GS	—
AlCl3-03	38.9	AlCl ₃ solution	3.5	40	37.8	1.8	—	—
det-02	39.1	Detergent solution	9.4	17	37.0	3.2	TS	3.8/3.4
det-03	38.9	Detergent solution	9.4	14	37.2	2.7	GS	—
det-04 ^a	38.8	Detergent solution	9.4	45	36.3	3.9	—	—

Note. All experiments were performed at 80 °C and a constant effective stress of 35 MPa; pH is measured at 80 °C; φ_c denotes porosity at the start of the creep phase; φ_f denotes porosity at the end of the creep phase; ε_f is the final creep strain; and TS and GS indicate samples used for thin section or grain size analysis, respectively.

^aRepresentative samples shown in Figures 3, 4, and 8.

washing in distilled water using a gravitational separation technique. The present 1-D compaction experiments were conducted on 5.01-g samples of this material.

To test the effect of chemical environment on compaction behavior, 11 different pore fluids were used as well as a low-vacuum (dry) environment, which served as a control environment (Table 1). The pore fluids used included three high-pressure supercritical phases, namely, N₂ (purity ≥ 99.999 vol%), CO₂ (purity ≥ 99.7 vol%) and water-saturated-CO₂ (wet CO₂). In addition, five chemically “simple” aqueous solutions were employed to test the effect of pH (HCl solutions of pH 1, 2.4, and 4; distilled water; and NaOH solution of pH 9), while three “complex” aqueous solutions were used to investigate the effect of solution composition independently of solution pH. These complex solutions consisted of a scaling inhibitor solution containing

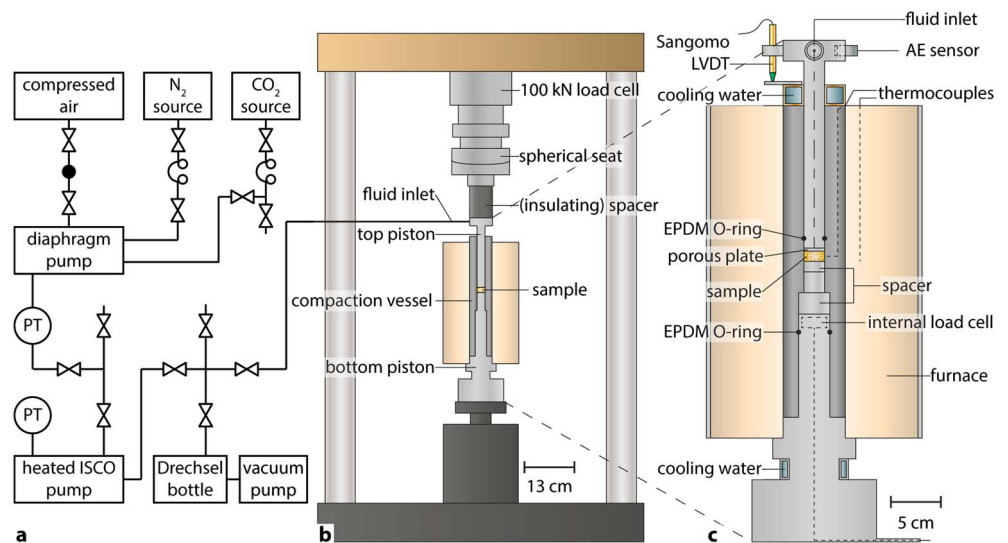


Figure 1. Overview of the experimental setup used in this study. (a) Pore fluid system including a diaphragm pump, servo-controlled ISCO pump, Dreschel bottle, and vacuum pump. Fluid pressure was measured with pressure transducers (PT). (b) Instron servo-controlled loading frame employed with a 100 kN load cell and (c) compaction vessel.

0.004 M AMP (amino trimethylene phosphonic acid; pH 2.5), 0.01 M AlCl_3 solution (pH 3.5), and simulated wastewater represented by a washing detergent solution (pH 9.4).

Low-vacuum (dry) conditions were obtained by evacuating the sample within the oedometer compaction vessel before and during mechanical testing, using a single-stage rotary vacuum pump (Figure 1a). The high-pressure fluids, N_2 , CO_2 , and wet CO_2 , were prepared in the ISCO pump and equilibrated overnight. After filling the ISCO pump with pure N_2 and CO_2 , the gases were prepressurized to 6 MPa using the diaphragm pump (Figure 1a). The externally heated ISCO pump was then used to achieve further pressurization to 10 MPa at 70 °C, resulting in supercritical conditions (Lemmon et al., 2018). Wet CO_2 was prepared by filling the ISCO pump (total volume 68 ml) with a small volume of water (10 ml) and completing the remaining volume with pure CO_2 . This mixture was prepressurized to 6 MPa using the diaphragm pump, and further pressurization to 10 MPa was achieved by the ISCO pump, while heating to 70 °C, yielding a water concentration of 54.39 mol of water per cubic meter (see section 4.2). All supercritical fluids were prepared at a lower temperature than the experimental conditions (80 °C) to prevent condensation of water in the upon injection into the sample.

Acidic solutions of pH 1, pH 2.4, and pH 4 were prepared by diluting fixed quantities of hydrochloric acid (HCl) in distilled water. The alkaline solution of pH 9 was prepared by diluting a fixed quantity of sodium hydroxide (NaOH) in distilled water. For the 0.01 M AlCl_3 solution, 2.4143 g of aluminum chloride salt was dissolved in 1 L of distilled water. The 0.004 M AMP solution was prepared by diluting 1‰ AMP solution with 1 L of distilled water. The washing detergent solution was prepared by mixing commercially available washing detergent powder (containing 5–15% anionic surfactants and <5% nonionic surfactants) with distilled water at a concentration of 6 g/L, the advised concentration for washing clothes. All aqueous solutions were stirred (>5 min) and left to equilibrate (>5 days) prior to use. After equilibration, each solution was heated to 80 °C to determine solution pH.

2.2. Experimental Setup and AE Monitoring System

The compaction experiments were performed in a uniaxial (1-D) compaction vessel (oedometer), loaded using an Instron 8862 servo-controlled loading frame (Figures 1b and 1c). The compaction vessel used is a modified version of the vessel originally described by Schutjens (1991) and later by Hangx et al. (2010), Brzesowsky, Hangx, et al. (2014), and Brzesowsky, Spiers, et al. (2014). The vessel and loading pistons are constructed from corrosion resistant Monel K-500, a copper-nickel-molybdenum alloy. The bottom piston

and vessel are secured on the Instron loading frame. The top piston contains a pore fluid bore, allowing both evacuation of the sample and injection of a pore fluid. The sand sample fills the bore of the vessel (20-mm diameter) between the upper and lower pistons, having a height of initially approximately 10 mm. A 1-mm-thick, porous, stainless steel plate between the top piston and sample ensures equal distribution of fluid over the sample cross-sectional area upon injection. In addition, it prevents grains from entering and clogging the pore fluid bore. The top and bottom pistons are sealed against the vessel wall using ethylene propylene diene monomer (EPDM) O rings.

Sample evacuation and fluid introduction are achieved via the pore fluid system (Figure 1a). This consists of a vacuum pump, Drechsel bottle, ISCO pump, diaphragm pump, and sources of compressed air, N₂ and CO₂. The vacuum pump is connected to the sample via the Drechsel bottle for evacuation of the sample. The diaphragm pump is used for prepressurizing the fluids in the ISCO pump at 6 MPa. The ISCO pump is used to achieve further pressurization to 10 MPa, while heating to 70 °C. Via the combination of valves shown in Figure 1, the sample can be directly connected to the ISCO pump to inject fluids prepared in the ISCO pump. Alternatively, the sample can be connected to the Drechsel bottle for flooding with aqueous solutions.

xial force, displacement, temperature, and pore fluid pressure are controlled and measured throughout the experiment. Force is applied by advancing the Instron loading ramp. It is measured externally using the Instron load cell (0 to 100 kN range, resolution ± 0.05 kN). In addition, force is measured with an internal load cell (0 to 100 kN range, resolution ± 0.05 kN) located in the top part of the bottom piston. Piston position and displacement are measured using linear variable differential transformers (LVDT) located in the Instron drive unit (± 50 mm range, resolution ± 0.25 μ m) and a Sangamo LVDT (± 1 mm range, resolution ± 0.1 μ m) located between the upper piston and the vessel (Figure 1c). A furnace allows controlled heating of the sample with ± 0.5 °C accuracy using a K-type chromel-alumel control thermocouple. This thermocouple is positioned within the furnace windings and connected to a proportional-integral-derivative controller. A second K-type thermocouple, embedded in the vessel wall adjacent to the sample, independently measures sample temperature. Pore fluid pressure was controlled and measured by the ISCO pump in the experiments employing supercritical fluids.

In addition, the experimental setup is equipped with an AE monitoring system that detects and counts AEs produced by the compacting sample. The AE events are detected using a ceramic piezoelectric resonator, mounted externally on the top piston (Figure 1c). The resulting signal passes through a precision preamplifier (36-dB gain) and a multistage signal conditioning system (24 dB gain). A 100 kHz to 1 MHz band-pass filter is applied to eliminate low-frequency interference and sensor resonance effects. Lastly, a two-channel counter with a constant trigger threshold of 200 mV, which is just above the noise level, discriminates and counts the incoming AE events. Pulse stretching times of 1,000 and 500 μ s are set for each counter, to check for wave packet arrival-bouncing effects and counter saturation. In the case of discrete events, the count rates from the two channels should be identical.

2.3. Experimental Procedure

Vessel assembly was conducted outside the Instron frame, first mounting the compaction vessel on its lower piston. A 10-mm-high stainless steel spacer was then inserted into the vessel to position the sample in the middle of the vessel, and a Teflon liner (10 mm high), sprayed externally with Molykote D-312R and dried for at least 1 hr, was emplaced to reduce friction between the sand sample and vessel wall. The sample material was then funneled into the vessel and the porous steel plate carefully placed on top of the sample using a guide rod. The furnace and top piston were subsequently added and the entire assembly located into the Instron loading frame.

In preparation for each experiment, the sample was heated to the target temperature of 80 °C, while simultaneously evacuating the sample assembly. After stabilization at 80 °C, which took approximately 1.5 hr, each sample was precompact by stress cycling, while continuously evacuating (Figure 2). First, a small stress of 0.3 MPa (equivalent to a force of 0.1 kN) was applied to the sample. The applied stress was then cycled at a constant stress rate of 5 MPa/min, following the sequence shown in Figure 2 (0.3–5–0.3–15–0.3–25–0.3–35–0.3 MPa). The aim of stress cycling was to condition each sample such that the variability in porosity between the different samples was reduced in preparation for

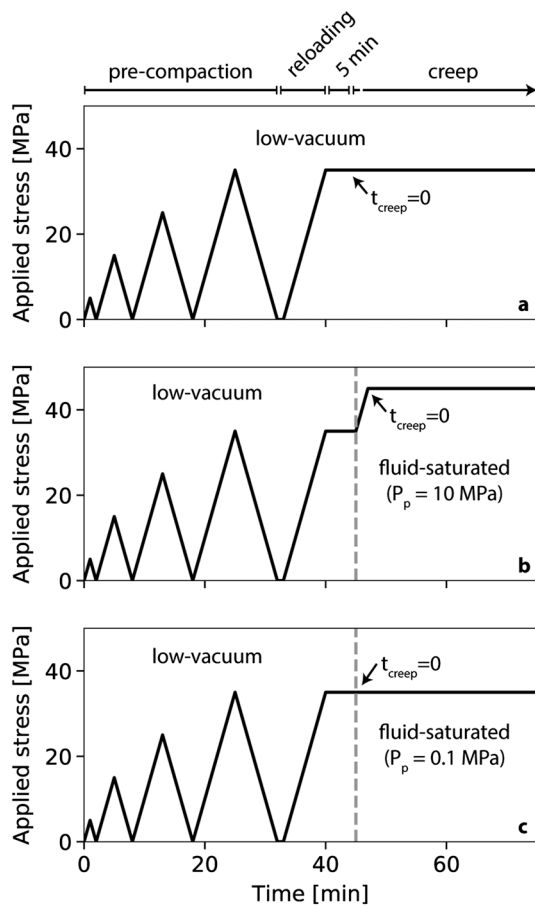


Figure 2. The experimental procedure for experiments performed at low-vacuum (dry) conditions (a), employed with supercritical fluids (b) or aqueous solutions (c). Precompaction stress cycling at low-vacuum (dry) condition is followed by reloading to 35 MPa and fluid addition in case of fluid-saturated experiments. The subsequent creep phase starts at $t_{\text{creep}} = 0$.

removed from the Instron loading frame and the sample carefully extracted. Samples tested with aqueous solutions were wet and cohesive, so remained intact. To improve their cohesion, selected dry and supercritical fluid charged samples (lc-01, dry-11, N₂-01, CO₂-01, CO₂-02, CO₂-03, wCO₂-04, and wCO₂-05) were vacuum flooded with distilled water prior to removal; this allowed them to be removed intact too. All wet samples were placed in an oven at 50 °C to dry for a minimum of 5 days prior to preparation for microstructural analysis.

2.4. Data Acquisition and Processing

Throughout each experiment, external Instron load, internal load, Instron LVDT position, Sangamo LVDT position, sample temperature, and cumulative AE counts were logged at an interval of 1 s. Applied axial stress and effective axial stress were calculated from the external Instron and internal load data, using pore fluid pressure data where relevant. Friction between the top piston seal and vessel wall was negligible for experiments conducted at atmospheric pressure and small (<0.6 MPa) for experiments with a pressurized pore fluid. This was not corrected for. Though measures were taken to reduce friction between the sand sample and vessel wall, comparison of external and internal load cell data indicated the occurrence of sample friction. For experiments performed with a pore fluid pressure, the stress measured by the internal load cell varied between 87.1% and 92.3% of the applied effective stress. For dry experiments and those performed with fluids at atmospheric pressure, the stress measured by the internal load cell was between 74.3% and 83.7% of the applied stress. Taking the sample stress as the average of the internally and externally

subsequent creep testing. This was done because compaction of sand aggregates is highly sensitive to the initial microstructure (Brzesowsky, Hangx, et al., 2014; Hangx et al., 2010).

After precompaction, evacuation continued and each sample was reloaded to 35 MPa at a stress rate of 5 MPa/min. This stress was held constant to observe the subsequent creep response in low-vacuum (dry) conditions or in the presence of supercritical fluids or aqueous solutions. For each chemical environment, two to four unique experiments were conducted to ensure reproducibility of the results (Table 1). The low-vacuum (dry) control experiments were evacuated for the entire experiment duration (Figure 2a). In the case of the fluid-saturated experiments, fluids were introduced 5 min after the constant stress of 35 MPa was applied. In experiments using supercritical fluids, these were introduced to the sample at 10 MPa. Once the fluid pressure had stabilized (within approximately 5 min), the applied stress was increased to 45 MPa, thus returning the axial effective stress to 35 MPa (Figure 2b). In the experiments using aqueous fluids, these were introduced at 1 atm by vacuum-flooding the sample (Figure 2c).

Creep was monitored throughout the experiments. For the low-vacuum (dry) experiments the creep phase started 5 min after the applied stress was 35 MPa ($t_{\text{creep}} = 0$ in Figure 2a), while for the experiments saturated with supercritical fluids it started as the effective axial stress returned to 35 MPa ($t_{\text{creep}} = 0$ in Figure 2b). Wetting of the sample, as evidenced by increased compaction, marked the onset of the creep phase in the experiments using aqueous solutions ($t_{\text{creep}} = 0$ in Figure 2c).

After one or multiple days (Table 1), the experiments were stopped. Low-vacuum (dry) experiments were terminated by completely unloading the sample and removing the vacuum. Supercritical fluid experiments were first unloaded to 35 MPa (25 MPa effective axial stress). After removing the pore pressure, the samples were then fully unloaded. The experiments employing aqueous solutions were completely unloaded in a single step. After unloading, the furnace was switched off and all samples were allowed to cool to room temperature. Subsequently, the assembly was

measured stress yields an average sample stress of $33.3 \text{ MPa} \pm 1.4\%$ for samples tested with pressurized pore fluids and $31.4 \text{ MPa} \pm 2.7\%$ for dry samples and samples saturated with a pore fluid at atmospheric pressure.

The starting length of the sample, that is, the sample length at t_{creep} (Figure 2), was determined by comparing the Instron LVDT position to an empty vessel reference point, at the same applied stress (35 MPa in dry and aqueous solution experiments and 45 MPa in supercritical fluid experiments). The Sangamo LVDT displacement data were corrected for elastic machine distortion using a predefined, eighth-order polynomial determined from machine calibrations on the experimental setup without sample. From the corrected Sangamo LVDT displacement data, instantaneous volumetric creep strain, defined as $e_v = -L/L_0$, was calculated, where L_0 is the length of the sample at the start of the creep phase and L is the change in length at any subsequent instant. Instantaneous strain rates, measured during the creep stage and defined as $\dot{\epsilon} = -(1/L)(dL/dt)$, were calculated by performing a least squares inversion over a variable time window centered around each individual displacement data point. The window size was based on a set tolerance for the uncertainty in displacement of $1 \mu\text{m}$, such that the error in the strain rate was always $\leq 0.01\%$. This method allowed for accurate determination of both high and low strain rates. Instantaneous AE rates were calculated similarly from the cumulative AE counts, with the tolerance for the AE window size set to 2,000 AE events.

2.5. Analytical and Microstructural Methods

After the experiments, grain size, microstructural, and crack density analyses were performed on selected samples, each having the same initial porosity and an experimental duration of 19 hr, where possible (Table 1). Grain size analysis on 1 g portions of selected samples and corresponding starting material was performed using a Malvern laser diffraction particle sizer. This allowed determination of the average grain size and grain size distribution before and after deformation. Despite the fact that laser particle size analysis systematically overestimates grain size by approximately 25%, due to fines adhering to coarse grains (Hangx et al., 2010; Pluymakers et al., 2014), the results are preferred here over optical analysis as these avoid the stereological uncertainty inherent to 2-D section study and sample a larger grain population.

Samples selected for microstructural and crack density analyses were impregnated with a low-viscosity, blue-dyed, epoxy resin (Araldite 2020) after drying. Thin sections were then cut parallel to the loading axis and analyzed using transmitted light microscopy. The blue-dyed resin resulted in a clear distinction between pores and quartz grains. Micrographs covering a field of 5 by 3 mm (50X magnification) were obtained from a selected area at the center of each thin section for crack density analysis.

Crack density analyses involved manual counting of cracks. All features that could be interpreted as cracks were considered. Crack resulting in the splitting of grains into two or three fragments were, where possible, inferred based on fragment size, shape, position, and extinction pattern in cross-polarized light. Very small grain fragments resulting from completely crushed grains were excluded from the analysis. The crack density in each selected area was determined using the linear intercept method (Wong, 1985), applied by superimposing a grid of orthogonal lines, with a 0.1 mm spacing, oriented parallel and perpendicular to the loading direction. The number of crack-line intercepts was counted and averaged for each orthogonal set, producing a linear intercept density (i.e., the number of crack intersections per unit length [mm^{-1}]) measured parallel (P_T^{\parallel}) and perpendicular (P_T^{\perp}) to the loading direction.

3. Results

3.1. Mechanical Data

For each tested environment, one representative experiment is selected based on sample porosity at the start of the creep phase ($t_{\text{creep}} = 0$ in Figure 2 and Table 1). The aim is to have a range in starting porosities that is as small as possible, so that there is a minimal effect of variations in the microstructure on compaction behavior between different samples. The porosity range of the representative samples is 38.7–39.0% for both the supercritical (Figure 3) and aqueous pore fluids (Figure 4) experiments. In general, all experiments were characterized by a rapid accumulation of strain in the first few minutes after loading, followed by ongoing creep at decreasing rate (cf. Figures 3 and 4).

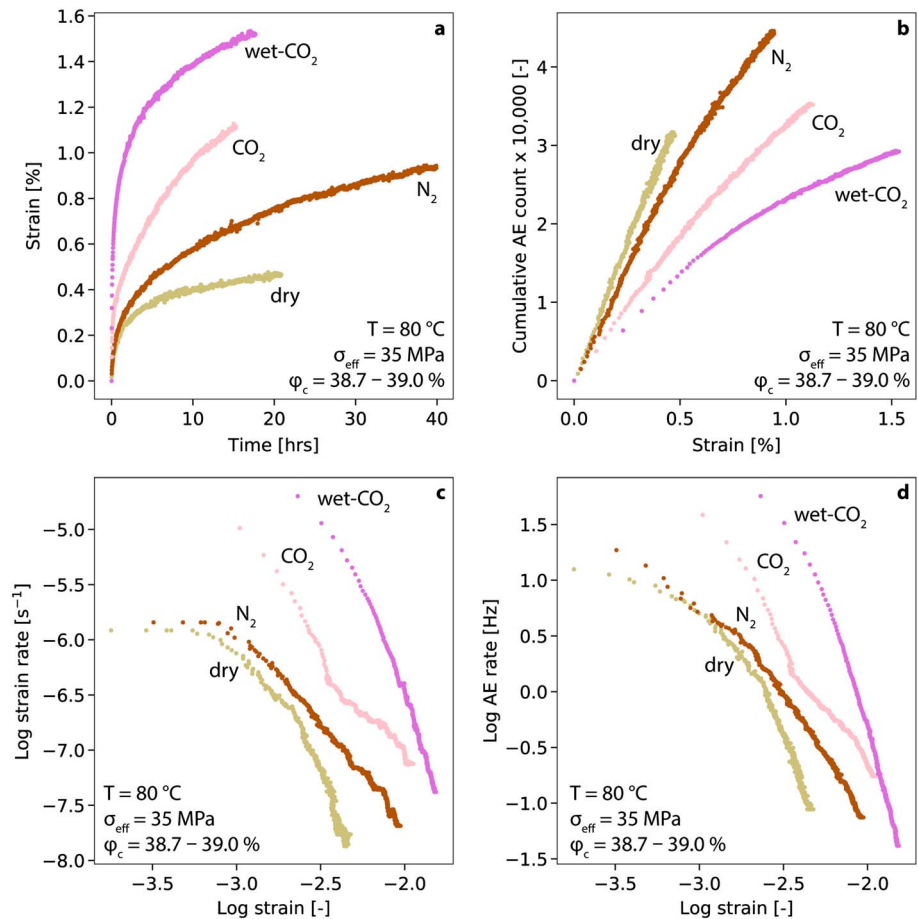


Figure 3. Representative data showing the effect of N₂, CO₂, and wet CO₂ on compaction creep compared with low-vacuum (dry) reference case. (a) Strain versus time plot and (b) cumulative acoustic emission count versus strain plot. (c) Strain rate and (d) acoustic emission rate are plotted as a function of log strain. T denotes temperature, σ_{eff} denotes effective stress, and ϕ_c denotes the porosity range of the selected samples at the start of the creep phase (see Table 1).

3.1.1. Low-Vacuum (Dry) Compaction Creep

In the first few minutes of creep, the representative control experiment conducted at low-vacuum (dry) conditions (dry-11) displayed about 0.2% strain, doubling to 0.4% strain in 15 hr, as illustrated in Figure 3a. During compaction, a total of approximately 32,000 AE events were recorded for this experiment (Figure 3b). At the start of the creep phase, typical strain rates of $10^{-5.9}\text{ s}^{-1}$ were registered, eventually decreasing to $10^{-7.8}\text{ s}^{-1}$ (Figure 3c). Similarly, the AE rate in the representative experiment decreased from $10^{1.1}$ to $10^{-1.1}\text{ s}^{-1}$ (Figure 3d).

3.1.2. Compaction Creep in the Presence of Supercritical Fluids

In general, supercritical fluids enhanced compaction relative to the representative dry control experiment (compare curves in Figures 3a and 3c). After 15 hr, the representative wet CO₂ experiment (wCO₂-05) produced the largest amount of compaction (1.5% strain), while the least deformation was observed in representative N₂ experiment (N₂-02; 0.7% strain). The selected CO₂ test (CO₂-01) resulted in an intermediate amount of strain of 1.1% after 15 hr. Surprisingly, the AE data showed the opposite trend (Figure 3b), with the lowest number of AEs occurring in the wet CO₂ environment (approximately 22,000 events) and the highest number of AEs occurring in the N₂-flooded experiment (approximately 43,000 events), at 0.9% strain. Experiments in N₂ environments showed only slightly faster strain rates compared to the low-vacuum (dry) experiments, with initial strain rates of typically $10^{-5.8}\text{ s}^{-1}$, reducing to $10^{-7.7}\text{ s}^{-1}$ by the end of the creep phase. Faster initial strain rates of typically $10^{-5.0}$ and $10^{-4.7}\text{ s}^{-1}$ were measured in experiments flooded with CO₂ and wet CO₂, ultimately falling to $10^{-7.1}$ and $10^{-7.4}\text{ s}^{-1}$, respectively. Similar trends were observed for

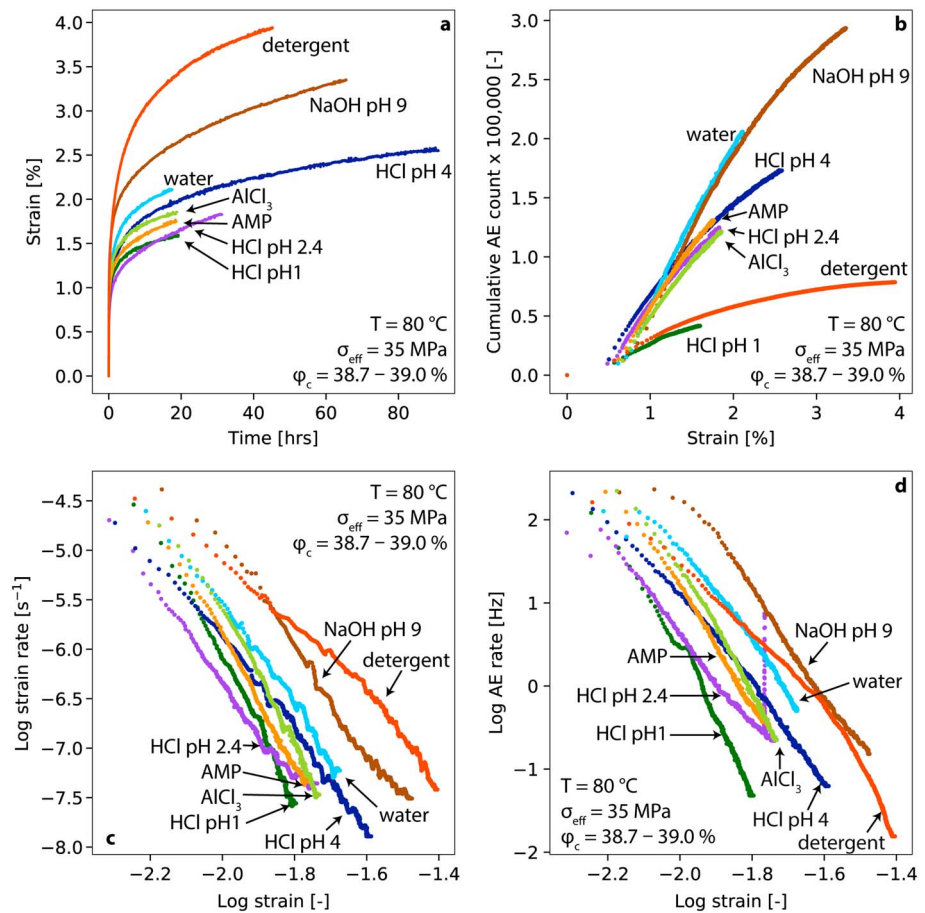


Figure 4. Representative data showing the effect of different aqueous solutions on compaction creep. (a) Strain versus time plot and (b) cumulative AE count versus strain plot. (c) Strain rate and (d) AE rate are plotted as a function of log strain. T denotes temperature, σ_{eff} denotes effective stress, and ϕ_c denotes porosity range of the selected samples at the start of the creep phase (see Table 1). Note the accelerated creep and AE rates compared with low-vacuum (dry) reference samples and samples flooded with supercritical fluids in Figure 3.

the AE rate data (Figure 3d). Overall, for a given amount of strain, saturation with N_2 resulted in the lowest creep strain rate and AE rates, while flooding with wet CO_2 resulted in the fastest creep strain and AE rates.

3.1.3. Compaction Creep in the Presence of Simple Aqueous Solutions

Wetting of the sample through addition of simple aqueous solutions resulted in more compaction compared to the low-vacuum control experiments and the experiments with supercritical fluids (cf. Figures 3a and 4a). Compaction was initially fast with indiscernible behavior for the different solutions during the initial 60 s, though clear differences in compaction behavior became apparent as compaction continued. A clear trend between total amount of strain and solution pH was noted, whereby low pH fluids (pH 1-2.4 solutions) lead to the least compaction and more creep strain was observed with increasing solution pH. For example, after 16 hr, the representative sample saturated with pH 1 HCl solution (1pH-04) exhibited 1.5% creep strain, while 2.6% strain was measured in a pH 9 NaOH solution (9pH-03; Figure 4a).

Representative samples tested with simple aqueous solutions exhibited strain rates of the order of $10^{-4.4}$ – $10^{-4.7}$ s^{-1} in the initial stages of creep (Figure 4c), which is faster than in the representative low-vacuum (dry) control and CO_2 and N_2 experiments, but similar to initial creep rates in the representative wet CO_2 environment (cf. Figures 3c and 4c). By the end of the creep phase in the simple aqueous solution experiments, strain rates of $10^{-7.2}$ s^{-1} and lower were measured. At a given strain and porosity, strain rates were generally slower in more acidic environments (low pH solutions) and increased with increasing solution pH. For example, at 1.6% strain ($10^{-1.8}$), the slowest strain rates were observed in representative

experiment employed with a pH 1 HCl solution ($10^{-7.6} \text{ s}^{-1}$), being approximately 1.5 orders of magnitude slower than the representative experiment flooded with pH 9 NaOH solution ($10^{-6.0} \text{ s}^{-1}$).

Compared to the low-vacuum (dry) environment, simple aqueous solutions resulted in a marked increase in the cumulative number of AE events (note the 1 order of magnitude difference in scale between Figures 3b and 4b). Moreover, alongside the tendering for strain and strain rate to increase with pH, more AEs and a higher AE rate were generally detected with increasing fluid pH. High initial AE rates, reaching up to 100 counts per second, were registered in the simple aqueous solutions experiments, which were faster than the representative control and CO₂ and N₂ experiments (cf. Figures 3d and 4d). Similar to the strain rate behavior, AE hit rates slowed down with accumulating creep strain, to typical values of 10^{-1} – 10^{-2} s^{-1} . AE rate trends as a function of pH were for a large part similar to the trends observed in the strain rate data. In the representative pH 2.4 HCl experiment (2.4pH-02), a sharp peak in AE rate is observed at approximately 1.7% strain ($10^{-1.8}$). Since no jump in displacement was measured, this peak is attributed to noise in the AE counting system.

3.1.4. Compaction Creep in the Presence of Complex Aqueous Solutions

Similar to the simple aqueous solutions, addition of complex aqueous solutions produced more creep strain and AEs, yielding higher creep strain and AE rates compared to experiments in low-vacuum (dry) conditions or with supercritical fluids (cf. Figures 3 and 4). Though complex aqueous solutions followed a similar pH trend with strain, AEs, creep strain, and AE rate as set out by the HCl and NaOH solutions, strains, AEs, and creep strain and AE rates were generally higher for the complex solutions compared their simple solution counterpart. For example, after 16 hr, 3.3% strain was measured in the representative washing detergent (pH 9.4) experiment (det-04) compared to 2.6% strain in the pH 9 NaOH experiment (9pH-03; Figure 4a). Controversially, all samples tested with washing detergent solution yielded a very low number of AEs (e.g., Figure 4b), while AE rates were within the order measured in samples saturated with distilled water or pH 9 NaOH solution (e.g., Figure 4d).

Creep strain rates measured in representative experiments with AMP (pH 2.5; AMP-03) and AlCl₃ solution (pH 3.5; AlCl3-01) were initially faster ($\dot{\epsilon} = 10^{-4.7}$ – $10^{-4.8} \text{ s}^{-1}$) than those measured in the representative pH 4 HCl experiment (4pH-03; Figure 4c). However, this initially more rapid compaction declined with increasing creep strain. After 1% (10^{-2}) and 1.6% strain ($10^{-1.8}$), the creep strain rates measured in the representative AMP and AlCl₃ experiments, respectively, decreased below those observed for the pH 4 HCl experiment. Similar to the creep strain rates, AE rates exhibited by the representative AMP and AlCl₃ experiments were initially faster than the representative pH 4 experiment and decreased below this reference at larger creep strains (cf. Figures 4c and 4d).

3.2. Grain Size and Microstructural Analyses

Grain size analysis and microstructural data for undeformed material and for samples compacted in low-vacuum (dry) conditions, with supercritical fluids and with aqueous solutions, are presented in Figures 5 and 6. Crack densities obtained from the samples analyzed are listed in Table 1.

Undeformed material consisted of subrounded grains and was marked by a narrow grain size distribution with a mean of 245 μm (see black curve in Figure 5a). Crack density analysis of a sample that was only subjected to precompaction stress cycling yielded $P_L^{\parallel} = 1.1 \text{ mm}^{-1}$ and $P_L^{\perp} = 1.1 \text{ mm}^{-1}$. Deformation under all conditions resulted in grain size reduction (Figures 5a and 6a) and the production of fine material with a grain size <80 μm (see Figures 5b and 6b). In all deformed samples, numerous cracks were observed. Most cracks fan from grain-to-grain contacts (cf. Figures 5c, 5d, and 6c–6f), both within grains (intragranular cracks) and across grain contacts (transgranular cracks), either with a divergent (spalling) or convergent (onion peel) nature. In addition, chipping of grain edges was observed and leading to the generation of very fine grained material (<10 μm). Cracks were homogeneously distributed throughout the samples, and no strain localization was observed. Crack density analysis indicated a slightly higher density of horizontal cracks, as crack densities measured parallel (P_L^{\parallel}) were generally higher than crack densities measured perpendicular (P_L^{\perp}) to the loading direction (Table 1).

3.2.1. Grain Size Reduction and Microcracking in Low-Vacuum (Dry) Conditions

Compaction creep at low-vacuum (dry) conditions reduced the overall grain size, resulting in a mean grain size of 230 μm for the sample selected for analysis. In addition, some fine material (<80 μm) was produced

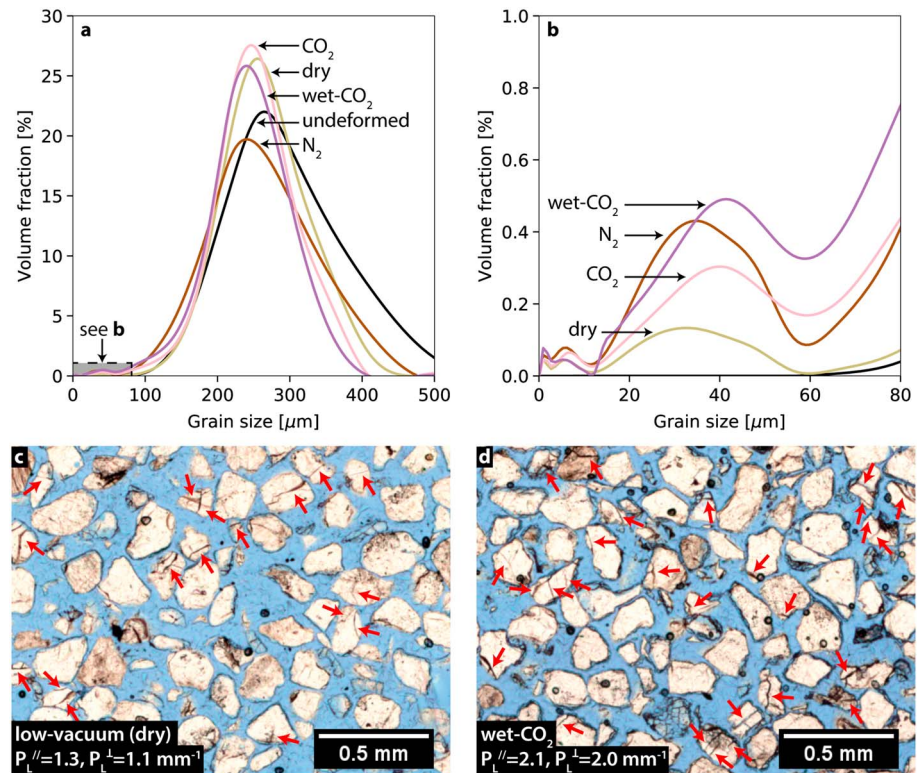


Figure 5. Grain size distributions and microstructures exhibited by samples subjected to uniaxial compaction creep with supercritical pore fluids. The grain size distribution is shown in (a), while (b) zooms in on the finest grain size fractions, that is, fines produced during compaction. Note that measured grain sizes are on average larger than the sieved grain sizes, which is due to a systematic overestimation by the Malvern particle sizer. Overall, the optical microstructures varied little and therefore only the extreme cases of (c) low-vacuum (dry) and (d) wet CO₂ are presented. Crack densities measured along grid lines superimposed parallel (P_L^{\parallel}) and perpendicular (P_L^{\perp}) to the loading direction are as shown. The loading direction is vertical and cracks are indicated by red arrows.

(Figure 5a). Microstructural analysis on the selected sample revealed crack densities of $P_L^{\parallel} = 1.3 \text{ mm}^{-1}$ and $P_L^{\perp} = 1.1 \text{ mm}^{-1}$ (Figure 5c).

3.2.2. Grain Size Reduction and Microcracking in the Presence of Supercritical Fluids

In line with the strain data for supercritical fluids, addition of wet CO₂ resulted in the largest grain size reduction (D50 = 213 μm) and fraction of fines (Figure 5b). In addition, significantly high crack densities were observed in the selected wet CO₂ sample ($P_L^{\parallel} = 2.1 \text{ mm}^{-1}$ and $P_L^{\perp} = 2.0 \text{ mm}^{-1}$; Figure 5d). Analysis of an experiment conducted with the CO₂ environment resulted in an intermediate mean grain size of 221 μm and low crack densities of $P_L^{\parallel} = 1.2 \text{ mm}^{-1}$ and $P_L^{\perp} = 1.1 \text{ mm}^{-1}$, which were similar to the low-vacuum (dry) experiment. The mean grain size exhibited after compaction creep in the N₂ environment was 215 μm, which may be slightly overestimated because of its relatively long creep duration of 40 hr. Crack densities measured on a N₂-saturated sample compacted for 19 hr were $P_L^{\parallel} = 1.3 \text{ mm}^{-1}$ and $P_L^{\perp} = 1.1 \text{ mm}^{-1}$.

3.2.3. Grain Size Reduction and Microcracking in the Presence of Aqueous Solutions

A similar trend with pH as observed for the strain data is reflected in the grain size and crack density data for the samples tested with aqueous solutions as pore fluid. Grain size reduction and crack density tend to increase with solution pH. Samples tested in the low pH environments pH 1 and pH 2.4 produced a relatively small amount of fine material (Figure 6b) and yielded high mean grain sizes of 220 and 221 μm and showed low crack densities of $P_L^{\parallel} = 1.7 \text{ mm}^{-1}$ and $P_L^{\perp} = 1.3 \text{ mm}^{-1}$, and $P_L^{\parallel} = 1.3 \text{ mm}^{-1}$ and $P_L^{\perp} = 0.8 \text{ mm}^{-1}$, respectively (Figure 6c). The pH 4 HCl solution and distilled water experiments had a moderate mean grain size of 213 and 215 μm and increased crack densities of $P_L^{\parallel} = 1.7 \text{ mm}^{-1}$ and $P_L^{\perp} = 1.4 \text{ mm}^{-1}$, and $P_L^{\parallel} = 3.4 \text{ mm}^{-1}$ and $P_L^{\perp} = 2.4 \text{ mm}^{-1}$ (Figure 6d), respectively. The lowest mean grain size was measured in

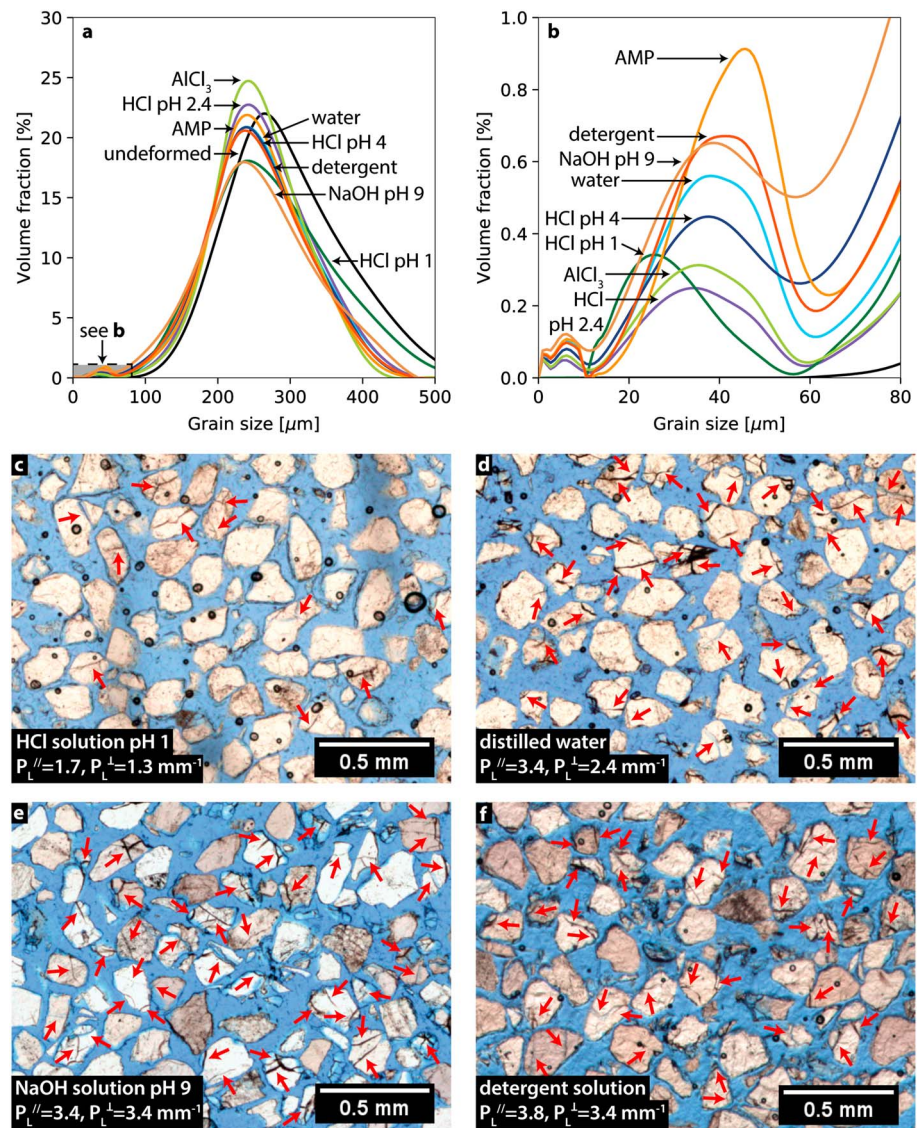


Figure 6. Grain size distributions and microstructures exhibited by samples subjected to uniaxial compaction creep with aqueous pore fluids. The grain size distribution is shown in (a), while (b) zooms in on the finest grain size fractions, that is, fines produced during compaction. Note that measured grain sizes are on average larger than the sieved grain sizes, which is due to a systematic overestimation by the Malvern particle sizer. A selection of samples spanning the whole of the tested pH spectrum are presented, including (c) pH 1 HCl solution, (d) distilled water, (e) pH 9 NaOH solution, and (f) washing detergent solution. Crack densities measured along grid lines superimposed parallel (P_L^{\parallel}) and perpendicular (P_L^{\perp}) to the loading direction are as shown. The loading direction is vertical and cracks are indicated by red arrows.

the sample flooded with pH 9 NaOH solution ($D_{50} = 205 \mu\text{m}$), which was also marked by a large production of fines (Figure 6b) and high crack densities ($P_L^{\parallel} = 3.4 \text{ mm}^{-1}$ and $P_L^{\perp} = 3.4 \text{ mm}^{-1}$; Figure 6e). The AMP solution experiment (pH 2.5) had a high percentage of fines (Figure 6b) and produced a mean grain size of $214 \mu\text{m}$ and crack densities of $P_L^{\parallel} = 2.5 \text{ mm}^{-1}$ and $P_L^{\perp} = 2.4 \text{ mm}^{-1}$, indicating more grain damage occurred in the AMP solution compared to the pH 2.4 HCl environment. The sample tested with AlCl_3 solution (pH 3.5) exhibited a mean grain size of $220 \mu\text{m}$ and crack densities of $P_L^{\parallel} = 1.9 \text{ mm}^{-1}$ and $P_L^{\perp} = 1.6 \text{ mm}^{-1}$, which are similar to the pH 4 HCl solution sample. For the washing detergent solution (pH 9.4), the mean grain size ($D_{50} = 211 \mu\text{m}$) was larger than the simple pH 9 NaOH solution, while crack densities ($P_L^{\parallel} = 3.8 \text{ mm}^{-1}$ and $P_L^{\perp} = 3.4 \text{ mm}^{-1}$) were similar (Figure 6f).

4. Discussion

The present uniaxial compaction experiments have shown that compaction creep of quartz sand aggregates is promoted by the presence of supercritical pore fluids and even more so by aqueous solutions, compared to low-vacuum (dry) conditions. The presence of all fluids employed resulted in higher strains, faster strain and AE rates, enhanced grain size reduction, and increased crack densities. Among the supercritical fluids explored, the effect on compaction creep was smallest under N_2 -saturated conditions, significant for pure CO_2 , and most pronounced under wet CO_2 -saturated conditions. In solution-flooded samples, a strong influence of solution pH on compaction behavior was observed, with very low pH environments ($pH \leq 3.5$) resulting in only small strains and few AEs, as well as slower strain and AE rates, limited grain size reduction, and low crack densities. As solution pH increases ($pH \geq 4$), a gradual increase in compaction and grain-scale cracking and damage occurs, with increasing grain size reduction. More complex solution compositions lead to compaction behavior that cannot be explained solely on the basis of solution pH, defined by the H^+ concentration.

4.1. Compaction Mechanisms in Dry and Fluid-Saturated Sand Aggregates

Prior to the creep phase, samples were stress cycled with increasingly larger stress steps applied at low-vacuum (dry) conditions (Figure 2). This resulted in strain hardening compaction and particle rearrangement with minor grain breakage, as evidenced by the relatively low crack density of the sample solely subjected to stress cycling, leading to a “locked” aggregate state at the maximum stress of 35 MPa applied. Additional deformation during the creep phase at this (effective) stress must have been accommodated by inelastic or permanent deformation of grains and/or grain contacts.

In general, mechanisms leading to inelastic deformation include (1) dissolution of grains due to undersaturation of the pore fluid with respect to the unstressed solid, (2) pressure solution at the grain contacts, (3) subcritical crushing of grain contacts, and (4) subcritical fracturing of the grains (Brzesowsky, Spiers, et al., 2014; F. M. Chester et al., 2007; J. S. Chester et al., 2004; Hangx et al., 2010; Karner et al., 2003; Niemeijer et al., 2002). In uniaxial compaction, these operate in series with intergranular slip (Takei et al., 2001). Dissolution or pressure solution features are not evident in our microstructures. In addition, strain rate calculations, based on the pressure solution model of Spiers et al. (2004) and on quartz dissolution rate data from Brady and Walther (1990) for a simple cubic pack of spherical grains, yield rates between 10^{-12} and 10^{-13} s^{-1} for dissolution-controlled pressure solution. Calculations for strain rates generated by dissolution of the quartz grains due to undersaturation of the pore fluid with respect to the solid yield rates in the same order of magnitude. These predicted strain rates are 4 to 8 orders of magnitude lower than observed in our experiments. Therefore, dissolution and pressure solution are unlikely mechanisms for the observed compaction behavior.

On the other hand, there is widespread evidence for microcracking in both the AE and microstructural data. Plotting the crack density determined from the micrographs versus total creep strain shows a linear relation with a slope of approximately 1 (Figure 7a). Similarly, plotting for all experiments cumulative AE events versus strain after a maximum creep duration present in all experiments, that is, $t = 13 \text{ hr}$, (Figure 7b) also suggests a positive relationship. However, several experiments (all experiments saturated with CO_2 , wet CO_2 and washing detergent, one distilled water, one pH 1, and one pH 4 HCl experiment) show a relatively low number of AEs in Figure 7b, compared with the general AE versus strain trend. This might reflect other grain-scale mechanisms leading to compaction, such as dissolution processes or reduced intergranular friction. The microstructural work and order-of-magnitude calculations suggest that pressure solution is unlikely to have occurred in our experiments. Moreover, sliding between the sand grains is unlikely to be possible without some form of contact point failure or removal. Therefore, it seems likely that attenuation by the pore fluid impaired AE detection.

Wave attenuation in CO_2 and wet CO_2 could account for the low-number AEs registered in all CO_2 and wet CO_2 experiments. This is supported by wave velocity measurements that yielded a stronger increase in the relative bulk modulus in CO_2 -saturated sandstone samples compared to sandstone samples saturated with water or N_2 at the same conditions (Moghadam et al., 2016; Njiekak et al., 2013). In the experiments with a washing detergent environment, the low concentration of detergent will not significantly change the density or bulk modulus relative to water. However, foam or air bubbles trapped in a pore fluid can

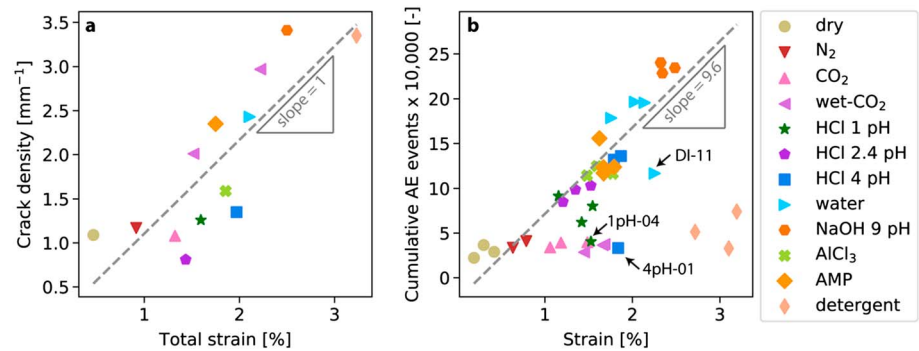


Figure 7. Crack density as determined from micrographs versus total creep strain for all experiments (a) and cumulative AE events versus strain after 13 hr of creep for all experiments (b).

attenuate seismic waves at low pore fluid pressures (<2 MPa; Tisato et al., 2015), such as the conditions imposed in our experiments, thereby impeding the AEs counts, resulting in an underestimation of AE events. Moreover, the wettability of quartz grain contacts may have been enhanced (Zdziennicka et al., 2009). We see no clear reason why attenuation would affect the outlying DI-11, 1pH-04, and 4pH-01 experiments that all contained water or HCl solutions (Figure 7b).

Excluding the aforementioned outlier data in Figure 7b, a linear relation between cumulative AE events and strain is observed. Performing linear least squares regression on the data sets results in approximately 960,000 AE per percent strain ($R^2 = 0.85$). Along this trend line, pore fluid pH increases, suggesting that increasing pore fluid pH enhances microcracking and indeed that compaction creep in our experiments is controlled by microcracking. Following grain or grain contact failure, grains and fragments presumably rearrange and contact stresses are redistributed. Similar inferences were made in previous studies on quartz sand compaction (Brzesowsky, Hangx, et al., 2014; Chuhan et al., 2002, 2003; Hangx et al., 2010; Nakata et al., 2001; Schutjens, 1991; Takei et al., 2001).

In crystalline materials, like quartz, microcracking occurs via the growth of cracks originating from surface flaws. From fracture mechanics theory, it is predicted that surface flaws propagate when the stress intensity at the crack tip attains the critical stress value (K_{IC} ; Griffith, 1921; J. Zhang et al., 1990). If the initial flaw length is much smaller than the grain size, surface flaws at the margin of the grain contact points are subjected to the Hertzian maximum tensile radial stress (Hertz, 1882). The stress field at the crack tip is then given by the mode I (opening mode) stress intensity factor $K_I = Y\sigma_r(\pi c)^{1/2}$, where Y is a dimensionless factor equal to 1.12 for an edge crack, σ_r is the remotely applied stress, and c is the half length of the flaw or crack (Atkinson, 1984; Brzesowsky, Hangx, et al., 2014; Frank & Lawn, 1967; J. Zhang et al., 1990). Critical or equilibrium crack growth occurs when the flaw size is equal or larger than the critical size and $K_I = K_{IC}$, resulting in grain failure.

However, under favorable temperature, pressure, and chemical conditions, cracks can grow subcritically (i.e., with $K_I < K_{IC}$), via stress corrosion, dissolution, diffusion, ion exchange, and microplasticity (Atkinson, 1984). In humid or wet environments, stress corrosion is classically inferred to be the main mechanisms controlling subcritical crack growth (Atkinson & Meredith, 1981; Dunning et al., 1994; Fisk & Michalske, 1985; Michalske & Bunker, 1984). Stress corrosion cracking in quartz involves the rupture of strained Si–O bonds at the crack tip and proceeds at the molecular level by similar pathways to dissolution (Dove, 1995). Furthermore, strained Si–O bonds are more reactive than unstrained ones, as shown by molecular dynamic simulations (Colombi Ciacchi et al., 2008; Lindsay et al., 1994; Silva et al., 2006; Y.-A. Zhang et al., 2014). Corrosive species such as water or hydroxyl groups attack the Si–O bonds via hydrolysis and replace them by silanol (SiOH) surface groups, according to the reaction



and



where < or > indicate surface-bound species (Charles, 1958; Dove, 1995; Xiao & Lasaga, 1994, 1996). The resulting silanol surface groups are weakly bonded via a hydrogen bond, which breaks more easily than the strong Si–O bond, allowing the crack tip to propagate at lower stress levels ($K_I < K_{IC}$; Michalske & Freiman, 1982).

Reactions (1) and (2) describe the end members of the solvent-surface interactions at the crack tip. The net crack growth rate is given by the relative contribution of each reaction via

$$r_{\text{Si-O}} = k_{\text{H}_2\text{O}}(\theta_{\text{H}_2\text{O}}) + k_{\text{OH}^-}(\theta_{\text{OH}^-}), \quad (3)$$

where k_i is the rate constant for bond rupture by H_2O or OH^- and θ_i is the surface site fraction of Si–O bonds reacting with H_2O or OH^- (Dove, 1995).

Stress corrosion cracking in glass and quartz has been extensively studied, and crack growth velocity has been found to be strongly influenced by temperature (Atkinson, 1984; Wiederhorn et al., 1980; Wiederhorn & Bolz, 1970), availability of water in the system (Atkinson, 1979; Michalske & Freiman, 1983; Scholz, 1972; Wiederhorn, 1967; Wiederhorn et al., 1982), and solution pH (Atkinson & Meredith, 1981; Dove, 1995; Dunning et al., 1984; Wiederhorn & Johnson, 1973). In the following, the observed compaction creep behavior and effect of chemical environment (supercritical fluids, simple, and complex aqueous solutions) are analyzed against this background.

4.2. The Influence of Supercritical Fluids on Compaction Creep

Saturation of our quartz sand samples with supercritical fluids (N_2 , CO_2 , or wet CO_2) had a fluid-specific response in terms of the amount and rate of strain and of AE, grain size reduction, and crack density, compared to a low-vacuum (dry) environment (Figures 3 and 5). Increasing strain and rates are observed progressing from N_2 as pore fluid to CO_2 and wet CO_2 , which cannot be related to the small difference in average stress experienced by the different samples, whereas stress corrosion cracking occurs via the rupture of weakened Si–O bonds due to water or hydroxyl attack, and N_2 and CO_2 have no such effect as their molecular structure does not favor adsorption onto or cleavage of the strained Si–O bond (Michalske & Bunker, 1984; Michalske & Freiman, 1983). However, small amounts of water (>0.2% relative humidity) can already accelerate crack growth velocities in glass, and faster rates are observed with increasing the relative humidity (Wiederhorn, 1967). Therefore, it is possible that trace amounts of water dissolved in the “pure” N_2 and CO_2 fluids used in our experiments aided stress corrosion. The water content of our N_2 and CO_2 environments was constrained by the impurity content of the source gas bottles, which is at maximum 5 and 150 ppm (volume fraction) water, respectively. Taking these maximum values, it can be inferred that the “dry” N_2 environment contained up to 0.27 mol of water per cubic meter and the “dry” CO_2 environment up to 8.17 mol of water per cubic meter (water density 54,514 mol/m³ (Lemmon et al., 2018)) at 70 °C and 10-MPa pore pressure. In the wet CO_2 fluid at the same conditions, up to 54.39 mol of water cubic meter should have been dissolved in the supercritical CO_2 phase (Duan & Zhang, 2006; CO_2 density 5,629.9 mol/m³ (Lemmon et al., 2018)). By contrast, samples subjected to the low-vacuum environment should have been devoid of water.

To assess the impact of water content on the compaction behavior of our quartz sand samples, we plotted strain and strain rate versus the above pore fluid water concentration for the low-vacuum (dry) and supercritical fluids bearing experiments and taking the molar density of water for the distilled water saturated experiments (Figures 8a and 8b). At each selected time, strain increases with water content. Similarly, for each plotted strain value, strain rates increase with water content. These trends qualitatively fit with the reported effect of relative humidity on crack growth velocity in glass (Wiederhorn, 1967). In addition, they are qualitatively consistent with the rate model for crack propagation in quartz developed by Dove (1995), which postulates that the rate of crack growth depends on the fraction of surface sites reaction with the corrosive species (equation (3)). In environments with a relatively high water content (e.g., wet CO_2 and distilled water), the concentration of water at crack tips will increase so that the reaction frequency between water and the Si–O bonds ($k_{\text{H}_2\text{O}}$) at crack tips intensifies, enhancing crack growth and, in the present case, sand grain or grain contact failure and hence compaction. Triaxial compression experiments on packs of

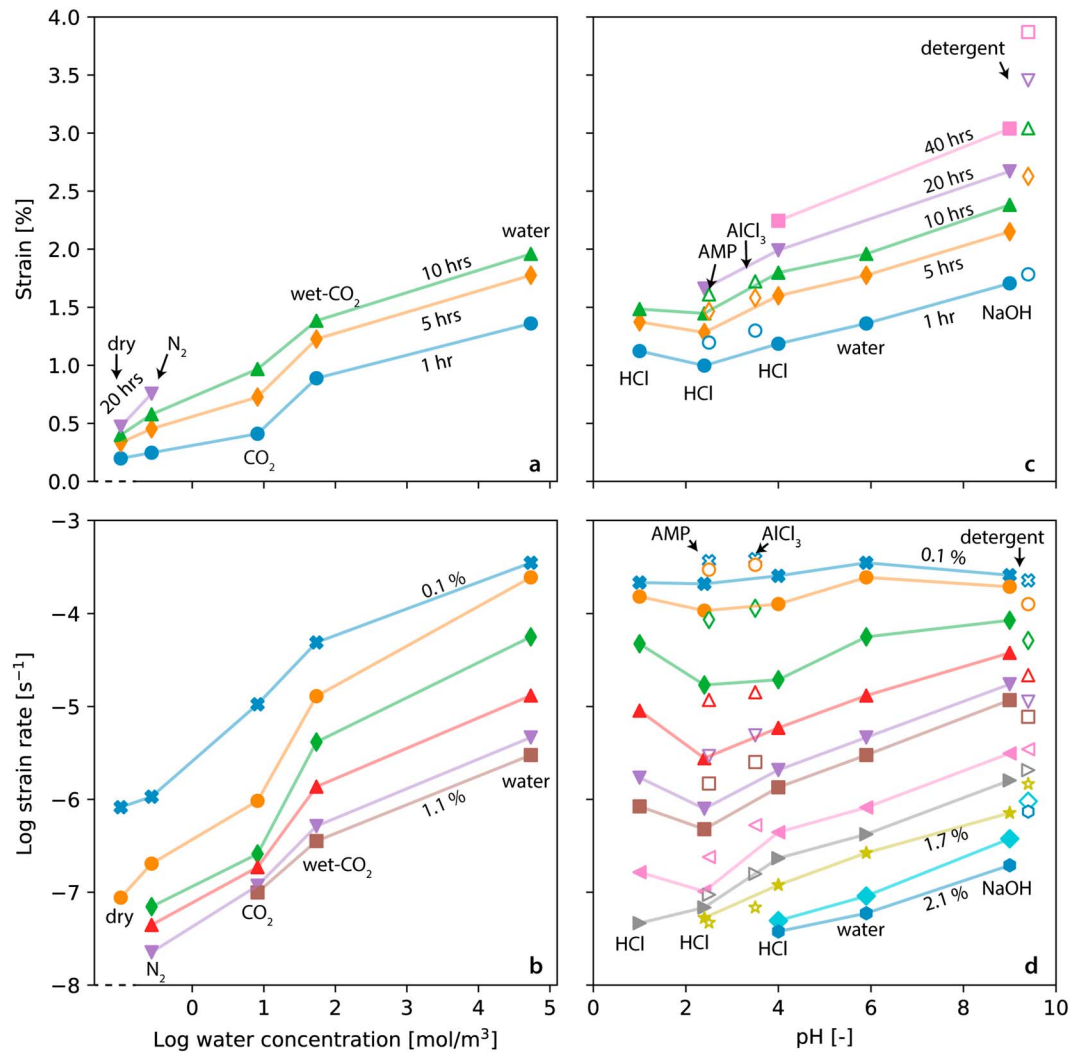


Figure 8. The change of strain and strain rate with time and strain, respectively. Panels (a) and (b) plot strain and strain rate versus the logarithm of water content for the supercritical fluids and distilled water experiment (see text). Panels (c) and (d) plot strain and strain rate versus pH for the aqueous solutions. Strain is plotted for several moments in time. Strain rates are plotted for several levels of strain; each line represents a strain increment of 0.2%. In (c) and (d), solid symbols represent simple solutions, that is, HCl solutions (pH 1, 2.4, and 4), distilled water, and 9 pH NaOH solution, and open symbols represent complex solutions, that is, solutions containing AMP (pH 2.5), AlCl₃ (pH 3.5), or washing detergent (pH 9.4).

loose granular novaculite and St. Peter sand (F. M. Chester et al., 2007) underpin this, as they showed a systematic increase in volumetric strain rate going from a dry environment to one containing water vapor and eventually being fully water saturated.

4.3. The Influence of Aqueous Solutions on Compaction Creep

4.3.1. Simple Acidic and Basic Solutions: The Effect of pH

Our results show that compaction of quartz sand is strongly influenced by pore fluid pH (Figures 8c and 8d), which do not relate to the small differences in average sample stress. At the times plotted in Figure 8c, strain increases with pH, though a minimum in strain is observed around pH 2.4. Similarly, at the selected strains and hence similar porosities shown in Figure 8d, strain rates increase with pH, except at the beginning of the experiments (0.1% and 0.3% strain), where a weaker dependence on pH is seen, especially at high pH.

The observed sensitivity of compaction creep behavior to solution pH is again qualitatively similar to the behavior found in studies of subcritical crack growth velocities in glass and quartz, where crack growth velocities increase with increasing solution pH above pH 4 and remain roughly constant below pH 2 (Atkinson & Meredith, 1981; Dove, 1995; Dunning et al., 1984; Wiederhorn & Johnson, 1973). Crack

growth velocities are related to access and attraction of corrosive species (H_2O and OH^-) to the crack tip. The force of attraction depends on the degree of ionization of the quartz surface, that is, the surface charge, which depends on solution pH (Dove & Elston, 1992; Du et al., 1994; Nangia & Garrison, 2008; Parks, 1984). At the pH point of zero charge (pH_{PZC}), which for quartz lies in the range of 2–3 (Kosmulski, 2018; Parks, 1965), the quartz surface is neutrally charged and covered by an electrically equivalent number of positively (SiOH_2^+) and negatively (SiO^-) charged surface groups (Parks, 1965). At $\text{pH} > \text{pH}_{\text{PZC}}$, negative groups dominate the quartz surface, resulting in a negative surface charge, while at $\text{pH} < \text{pH}_{\text{PZC}}$, the surface charge is positive due to the abundance of positively ionized surface groups. The charged quartz surfaces attract corrosive species such as H_2O and OH^- more strongly than neutrally charged surfaces, resulting in increased activity at the crack tip and faster crack growth velocities. Though our experiments were conducted at an elevated temperature, the pH_{PZC} is expected to be relatively insensitive to temperature (Sverjensky & Sahai, 1998). In addition, crack velocities in alkaline solutions increase beyond those seen in neutral or acidic solutions due to the abundance of OH^- , which is a stronger corrosive species than water (Casey et al., 1990; Dove, 1995) due to its free electron, enhancing hydrolysis, and breakage of the Si–O bond (Michalske & Freiman, 1982, 1983). Hence, the trends in strain and strain rate versus pH seen in Figures 8c and 8d match well with the expected effects of pH on subcritical crack growth rates at sand grain contacts.

On this basis, our overall inference is that the main mechanism controlling compaction creep in our quartz sand samples in the presence of simple aqueous solutions was pH-controlled subcritical crack growth, coupled with subsequent grain rearrangement. This is in accordance with previous studies on quartz and feldspar sand (Hangx et al., 2010).

4.3.2. The Effect of Additives in Complex Solutions

We now consider the effects of pore fluids containing AMP (pH 2.5), AlCl_3 (pH 3.5), and washing detergent (pH 9.4) additives. Each of the solutions has a pH similar to one of the simple HCl or NaOH solutions used in this study, so that the effect of these additives on compaction creep could be investigated independently of purely pH effects. For this purpose, the strain and strain rate data obtained for samples tested using these complex solutions are added, using open symbols, to Figures 8c and 8d.

Overall, these data show that the complex additives tended to lead to higher creep strains and higher creep strain rates at a given pH. Compaction in the presence of either AMP or AlCl_3 solution initially increased strain by 20% and 8%, respectively, relative to compaction in presence of a simple aqueous solution of similar pH. With time this difference decreases and eventually vanishes for the AlCl_3 solution after 10 hr (Figure 8c). Similarly, pore fluids containing AMP or AlCl_3 supported strain rates that were initially faster than expected based on solution pH. However, by 1.7% strain, strain rates slowed to values below those observed using HCl/NaOH solutions (Figure 8d). In the presence of washing detergent solution with pH 9.4, strains were always larger than measured using the reference NaOH solution (pH 9), with the difference increasing with time (Figure 8c). Strain rates were initially slower than expected based on solution pH but beyond 1.5% strain became faster (Figure 8d).

The overall creep enhancing effect of the additives compared to their simple solution counterpart suggests that the chemical nature of the additive promotes additional subcritical crack growth. Quartz dissolution rates are enhanced in the presence of cations (Dove & Crerar, 1990; Dove & Elston, 1992; Dove & Nix, 1997; Kubicki et al., 2012; Tamada et al., 2012; S. Zhang & Liu, 2014) and organic acids (Bennett et al., 1988). At $\text{pH} > \text{pH}_{\text{pzc}}$, attraction of cations to the negatively charged quartz surface disturbs the surface structure by lengthening the Si–O bond and opens the bond angle (Dove & Crerar, 1990). This permits corrosive species to approach and attack the Si–O bonds more readily. This has been inferred to be the main mechanism by which Na^+ can enhance compaction creep rates in quartz and feldspar aggregates in the presence of NaCl solutions at pH values in the range 5.5–7 (Brzesowsky, Hangx, et al., 2014; Hangx et al., 2010).

In the experiments performed using AMP solution (pH 2.5), the pH is very close to the pH_{pzc} of quartz and the reactivity of the almost neutrally charged quartz surface with other species is minimal (Dove & Elston, 1992). AMP is a weak acid (Tantayakom et al., 2005). Ordered around a central nitrogen atom within the AMP molecule are three methylene phosphate groups, each containing two hydroxyl groups available for deprotonation (Tantayakom et al., 2005). Due to incomplete dissociation, not all six groups release protons into solution, leaving some hydroxyl groups for interaction with the quartz surface. We argue that though the acid nature of the AMP solution will inhibit microcracking compared to distilled water, the presence

of corrosive hydroxyl groups in the AMP molecule enhances crack growth compared to the simple HCl solution of similar pH. Though this is speculation, molecular dynamics simulations, similar to the work of Kubicki et al. (2012) and Zhang and Liu (2014), could potentially demonstrate this.

In case of the AlCl_3 solution (pH 3.5), the quartz surface charge is slightly negative, attracting the Al^{3+} cations present in solution. Previous work (Iler, 1973) has shown that these cations adsorb onto the quartz surface to form Al–O surface groups, which are likely positively charged in the pH 3.5 environment, as the pH_{PZC} for Al–O groups is approximately 5–9 (Parks, 1965). Following Du et al. (1994), the disordered interface then allows water to approach the quartz surface more easily. In addition, it may be argued that the positively charged Al–O groups attract the few hydroxide ions present in solution at pH 3.5, which more strongly attack the quartz surface than do water molecules.

In the pH regime of the washing detergent solution (pH 9.4), the quartz surface is very reactive (Dove, 1995). The larger strain and strain rates measured using this fluid, compared to the pH 9 NaOH solution, suggests that the washing detergent components perturb the solvent structure at the quartz interface. The detergent solution contains anionic surfactants, which are not attracted to the negatively charged quartz surface. On the other hand, the detergent also contains zeolites, which carry cations such as Na^+ , K^+ , Ca^{2+} , and Mg^{2+} in their porous structure. It was reported that Na^+ can be released into solution via a cation exchange reaction with H^+ (Boyd et al., 1947) and may subsequently interact with the quartz surface as described by Dove and Crerar (1990), presumably enhancing crack growth and compaction creep.

4.4. Implications

The compaction creep experiments presented in this study show that creep of quartz sand aggregates due to grain and grain contact failure by stress-corrosion cracking is strongly influenced by pore fluid chemistry, that is, by water content or activity, solution pH, and added solute species. The observed effects may be extended to the compaction creep of sandstones, when subcritical crack growth controls deformation. Previous workers have shown that microcracking is an important mechanism in sandstone deformation high stresses and strains (Heap et al., 2009; J. Zhang et al., 1990) and the presence of water leads to a pronounced weakening effect (Baud et al., 2000; Hu et al., 2017, 2018). This suggests that, compared to the behavior of quartz sands, sandstones respond similarly to changes in water content and solution pH and presumably to the introduction of additives such as those studied here. However, sandstones are cemented by and contain other minerals, such as feldspars (Hangx et al., 2010), carbonates (Liteanu et al., 2012), and clays. In detail, therefore, changing the pore fluid chemistry may influence the compaction creep behavior differently from a pure granular quartz system, as each mineral has its own pH_{PZC} and hence a different pH dependence of crack growth and dissolution behavior. In addition, the quartz grain size and the minerals cementing a sandstone (i.e., calcite or quartz) will influence crack growth velocity, trajectory, and hence grain failure mode and creep rate (Rijken, 2005). Other creep processes may also operate. Time-dependent fluid-rock interactions at the sample scale in CO_2 -saturated sandstone have been extensively analyzed (e.g., Rohmer et al., 2016), but a systematic study of the effect of other fluids on the time-dependent deformation of sandstone is lacking.

Our experiments were performed at stress and temperature conditions similar to those pertaining to depleted sandstone gas reservoirs at 2 to 4 km depth. Even after substantial depletion, the state of stress in such reservoirs remains far below the range required for yield by widespread grain crushing (i.e., below the so called P^* value or conventional yield point C^* ; see Pijenburg et al., 2018, 2019). This implies that the grain-scale mechanisms operating in our sand samples may also operate during compaction of depleted reservoirs but at lower rates due to the lower porosities and hence lower grain contact stresses that characterize sandstones as opposed to loose sands. The creep strain rates measured in our study are 4–7 orders of magnitude faster than total reservoir compaction rates (i.e., elastic plus inelastic/creep rates) related to pore pressure depletion, which are approximately 10^{-12} s^{-1} for depleted reservoirs in the Po Basin, Italy (Ferronato et al., 2010; Menin et al., 2008), and the Groningen reservoir in the Netherlands (NAM, 2015), as calculated from surface subsidence data. However, the relative effects of changes in pore fluid chemistry on compaction creep seen in our experiments provide insight into the potential effects of such changes on the creep of sand and sandstone reservoirs under depletion and postdepletion conditions.

Assuming compaction of both unconsolidated sand and sandstone reservoir rocks is controlled by microcracking in quartz grains or quartz-rich cement, the results of this study may point to a potential strategy for mitigating reservoir compaction resulting from creep following or associated with natural gas production or even geothermal energy production. Depleted gas reservoirs are not devoid of fluids but partly saturated with site-specific formation water, which is a combination of the original formation water and ingress water from adjacent formations injected during stimulation activities. A gas or supercritical fluid at reservoir conditions, such as N_2 or CO_2 , could perhaps be injected into the reservoir to mitigate compaction creep through pressure restoration or maintenance. Injection can locally dry the reservoir, as formation water will dissolve into the supercritical fluid, or else the supercritical fluid may displace the formation water, resulting in N_2 - or CO_2 -saturated pores. As shown in this study, supercritical fluids like N_2 and CO_2 inhibit compaction creep of quartz sand relative to aqueous solutions due to reduced chemical interaction with water (cf. Figures 8a and 8b), so that alongside pressure restoration effects, injection of these fluids might help mitigate compaction creep after natural gas production. Injection of CO_2 has the added advantage of reducing anthropogenic CO_2 emissions (IPCC, 2005) and reducing pore water pH hence inhibiting stress corrosion cracking. However, care needs to be taken when considering pressure restoration to avoid induced seismicity. While increasing pore fluid pressure and lowering the effective stress reduce the driving force for reservoir compaction, N_2 and CO_2 injection will also change the stresses acting on any nearby faults and possible expansion of the reservoir may lead to (reverse) fault motion (Ellsworth, 2013). Fault friction or creep might also be affected through chemical interactions (Samuelson & Spiers, 2012).

Alternatively, aqueous solutions can be injected into reservoirs at lower pressures, with the aim of reducing the pH of the formation water or to introduce creep-inhibiting additives. Little data are available on the pH of formation waters, though for moderately saline waters it is believed to vary between 7 and 9, while for highly saline water it can be as low as 3 (Case, 1945; Hanor, 1994). Though this range is very broad, it is far from the optimal pH of 2.4 (in pH_{pzc} range), where observed compaction rates were slowest (Figure 8d). In principle, formation fluid pH could be lowered in some cases by injecting an HCl-rich fluid into a quartz sand or sandstone reservoir, provided the carbonate content is low. Another potential agent is AMP, as it reduces compaction creep compared to distilled water, though not as effectively as an HCl solution with the same pH. AMP has the advantage that it is already used as a scaling inhibitor in drinking water facilities and is an environmentally safe additive.

In all of the above scenarios, mitigation of reservoir compaction via fluid injection is only feasible when it can be done in a geomechanically and environmentally safe way. Multiple hazards are associated with fluid injection, including leakage, induced seismicity, and reservoir deformation, which can have consequences for the atmosphere, surface, and subsurface environment (Schimmel et al., 2019). Before any injection operation in a high uncertainty system like the subsurface can be implemented, these hazards and their consequences need to be considered, including their potential interplay, to create a throughout understanding of the cumulative risks.

As a final remark, this study shows that the injection of alkaline solutions or solutions containing detergent is better avoided in porous sandstone reservoirs as it enhances compaction. Wastewater injection is very common in enhanced oil recovery operations and during the production of shale gas. Besides increasing the pore pressure, which can (re)activate faults (Ellsworth, 2013), these injection fluids also contain detergents that can promote compaction creep. In addition, pore fluid chemistry may affect fault gouge properties and hence fault stability (Dunning et al., 1994). Though there are many types of detergents and these findings may not be applicable to all, care has to be taken regarding the injection of fluids with an alkaline composition into sands and sandstones.

5. Conclusions

This paper focused on investigating the effect of changes in pore fluid chemistry on the 1-D compaction creep behavior of quartz sand aggregates. Systematic uniaxial constant stress experiments were performed at 35 MPa effective stress and 80 °C, that is, at realistic in situ reservoir conditions. The effect of chemical environment was tested, using a low-vacuum (dry) environment, three supercritical fluids (N_2 , CO_2 , and wet CO_2) at 10 MPa pore pressure, five simple aqueous solutions (HCl solutions of pH 1, 2.4, and 4, distilled water, and NaOH solution of pH 9) added at atmospheric pressure, and three complex aqueous solutions

(AMP solution of pH 2.5, AlCl_3 solution of pH 3.5 and washing detergent solution of pH 9.4) also added at atmospheric pressure.

The following effects of chemical environment were observed:

1. Compaction creep under low-vacuum (dry) conditions was slow and resulted in relatively small strains, slow strain and AE rates, a small reduction in grain size, and a low crack density.
2. Introduction of supercritical fluids enhanced compaction creep compared to dry conditions. The smallest effect was observed in the presence of N_2 and the largest effect in the presence of wet CO_2 . Though AEs were attenuated in the supercritical fluids, microstructural analysis evidenced increased grain breakage for N_2 , CO_2 , and wet CO_2 , suggesting that microcracking controlled compaction creep.
3. Addition of aqueous solutions promoted compaction creep compared to both dry and supercritical conditions. A clear trend with pH was observed, whereby compaction, strain and AE rates increased with solution pH for $\text{pH} > 2.4$. Complex additive solutions invoked more compaction and faster creep strain and AE rates compared to their simple solution counterparts with the same or similar pH. Microstructural analysis indicated that microcracking was the dominant deformation mechanism.
4. It was inferred that compaction creep in quartz sand aggregates is controlled by subcritical crack growth with subsequent rearrangement of grains and grain fragments. The observed effects of chemical environment were further inferred to be related to changes in activity of corrosive species (H_2O and OH^-) at the crack tip. In the case of the supercritical fluids, increased water content (wet $\text{CO}_2 > \text{CO}_2 > \text{N}_2$) was inferred to increase water availability and accessibility to the crack tip, thereby enhancing subcritical crack growth. In aqueous solutions at $\text{pH} > \text{pH}_{\text{pzc}}$, corrosive species are inferred to be attracted to the quartz surface due to the surface charge, which is likely to promote crack growth. Moreover, in alkaline solutions the strong corrosive OH^- ion is abundant, which is inferred to further enhance creep.
5. Additives in the complex aqueous solutions are also attracted to the crack tip where, following previous work, they perturb the solvent structure at the quartz surface, by stretching and opening the Si–O bond. This is thought to improve the accessibility of the corrosive species to the Si–O bond, increasing the reaction frequency, which is inferred to promote crack growth and hence compaction creep.
6. Assuming subcritical crack growth also controls reservoir compaction, the present results may point to potential strategies for mitigating reservoir compaction via the injection of fluids. Locally drying the reservoir via the injection of gas or supercritical fluid may decrease the rate of compaction. Alternatively, injection of an acidic fluid to lower the formation water pH, such as CO_2 or AMP, can potentially inhibit compaction creep. On the other hand, injection of alkaline fluids, such as wastewater, is better avoided as it can accelerate compaction creep of porous sand and sandstone reservoirs.

Acknowledgments

This work is part of the research program Transitioning to a More Sustainable Energy System with project 022.004.023, which is financed by the Netherlands Organisation for Scientific Research (NWO). Declarations of interest: none. The technical staff of the HPT Laboratory is thanked for their assistance, especially Gert Kastelein, Eimert de Graaff, Thony van der Gonnetscher, and Floris van Oort. Leonard Bik is thanked for preparing the thin sections. We are thankful to Colin Peach and Tim Wolterbeek for assistance in the laboratory and constructive discussions. Martijn de van Ende is thanked for help with programming. We also thank two anonymous reviewers for their thoughtful feedback that helped to improve the manuscript. The data for this paper are available as Schimmel et al. (2019): Compaction creep data uniaxial compaction of quartz sand in various chemical environments. GFZ Data Services. <http://doi.org/10.5880/figeo.2019.005>.

References

- Atkinson, B. K. (1979). A fracture mechanics study of subcritical tensile cracking of quartz in wet environments. *Pure and Applied Geophysics PAGEOPH*, 117(5), 1011–1024. <https://doi.org/10.1007/BF00876082>
- Atkinson, B. K. (1984). Subcritical crack growth in geological materials. *Journal of Geophysical Research*, 89(B6), 4077–4114. <https://doi.org/10.1029/JB089iB06p04077>
- Atkinson, B. K., & Meredith, P. G. (1981). Stress corrosion cracking of quartz: A note on the influence of chemical environment. *Tectonophysics*, 77(1–2), T1–T11. [https://doi.org/10.1016/0040-1951\(81\)90157-8](https://doi.org/10.1016/0040-1951(81)90157-8)
- Bachu, S., & Gunter, W. (2005). Overview of acid-gas injection operations in Western Canada. *Greenhouse Gas Control Technologies*, 1(1), 443–448. <https://doi.org/10.1016/B978-008044704-9/50045-8>
- Baud, P., Zhu, W., & Wong, T. (2000). Failure mode and weakening effect of water on sandstone. *Journal of Geophysical Research*, 105(B7), 16371–16389. <https://doi.org/10.1029/2000JB900087>
- Bennett, P. C., Melcer, M. E., Siegel, D. I., & Hassett, J. P. (1988). The dissolution of quartz in dilute aqueous solutions of organic acids at 25°C. *Geochimica et Cosmochimica Acta*, 52(6), 1521–1530. [https://doi.org/10.1016/0016-7037\(88\)90222-0](https://doi.org/10.1016/0016-7037(88)90222-0)
- Bernabé, Y., Fryer, D. T., & Shively, R. M. (1994). Experimental observations of the elastic and inelastic behaviour of porous sandstones. *Geophysical Journal International*, 117(2), 403–418. <https://doi.org/10.1111/j.1365-246X.1994.tb03940.x>
- Boyd, G. E., Schubert, J., & Adamson, A. W. (1947). The exchange adsorption of ions from aqueous solutions by organic zeolites. I. Ion-exchange equilibria. *Journal of the American Chemical Society*, 69(11), 2818–2829. <https://doi.org/10.1021/ja01203a064>
- Brady, P. V., & Walther, J. V. (1990). Kinetics of quartz dissolution at low temperatures. *Chemical Geology*, 82, 253–264. [https://doi.org/10.1016/0009-2541\(90\)90084-K](https://doi.org/10.1016/0009-2541(90)90084-K)
- Brantut, N., Baud, P., Heap, M. J., & Meredith, P. G. (2012). Micromechanics of brittle creep in rocks. *Journal of Geophysical Research*, 117, B08412. <https://doi.org/10.1029/2012JB009299>
- Brzesowsky, R. H., Hangx, S. J. T., Brantut, N., & Spiers, C. J. (2014). Compaction creep of sands due to time-dependent grain failure: Effects of chemical environment, applied stress, and grain size. *Journal of Geophysical Research: Solid Earth*, 119, 7521–7541. <https://doi.org/10.1002/2014JB011277>

- Brzesowsky, R. H., Spiers, C. J., Peach, C. J., & Hangx, S. J. T. (2011). Failure behavior of single sand grains: Theory versus experiment. *Journal of Geophysical Research*, *116*, B06205. <https://doi.org/10.1029/2010JB008120>
- Brzesowsky, R. H., Spiers, C. J., Peach, C. J., & Hangx, S. J. T. (2014). Time-independent compaction behavior of quartz sands. *Journal of Geophysical Research: Solid Earth*, *119*, 936–956. <https://doi.org/10.1002/2013JB010444>
- Case, L. C. (1945). Exceptional Silurian brine near Bay City, Michigan. *AAPG Bulletin*, *29*, 567–570.
- Casey, W. H., Lasaga, A. C., & Gibbs, G. (1990). Mechanisms of silica dissolution as inferred from the kinetic isotope effect. *Geochimica et Cosmochimica Acta*, *54*(12), 3369–3378. [https://doi.org/10.1016/0016-7037\(90\)90291-R](https://doi.org/10.1016/0016-7037(90)90291-R)
- Charles, R. J. (1958). Static fatigue of glass. I. *Journal of Applied Physics*, *29*(11), 1549–1553. <https://doi.org/10.1063/1.1722991>
- Chester, F. M., Chester, J. S., Kronenberg, A. K., & Hajash, A. (2007). Subcritical creep compaction of quartz sand at diagenetic conditions: Effects of water and grain size. *Journal of Geophysical Research*, *112*, B06203. <https://doi.org/10.1029/2006JB004317>
- Chester, J. S., Lenz, S. C., Chester, F. M., & Lang, R. A. (2004). Mechanisms of compaction of quartz sand at diagenetic conditions. *Earth and Planetary Science Letters*, *220*(3–4), 435–451. [https://doi.org/10.1016/S0012-821X\(04\)00054-8](https://doi.org/10.1016/S0012-821X(04)00054-8)
- Chuhan, F. A., Kjeldstad, A., Bjørlykke, K., & Høeg, K. (2002). Porosity loss in sand by grain crushing—Experimental evidence and relevance to reservoir quality. *Marine and Petroleum Geology*, *19*(1), 39–53. [https://doi.org/10.1016/S0264-8172\(01\)00049-6](https://doi.org/10.1016/S0264-8172(01)00049-6)
- Chuhan, F. A., Kjeldstad, A., Bjørlykke, K., & Høeg, K. (2003). Experimental compression of loose sands: Relevance to porosity reduction during burial in sedimentary basins. *Canadian Geotechnical Journal*, *40*(5), 995–1011. <https://doi.org/10.1139/t03-050>
- Colazas, X. C., & Strehle, R. W. (1995). Chapter 6 subsidence in the Wilmington Oil Field, Long Beach, California, USA. In G. V. Chilingar, E. C. Donaldson, & T. F. Yen (Eds.), *Subsidence due to Fluid Withdrawal. Developments in Petroleum Science*, (Vol. 41, pp. 285–335). Amsterdam: Elsevier Science B.V. [https://doi.org/10.1016/S0376-7361\(06\)80053-1](https://doi.org/10.1016/S0376-7361(06)80053-1)
- Colombi Ciacchi, L., Cole, D. J., Payne, M. C., & Gumbsch, P. (2008). Stress-driven oxidation chemistry of wet silicon surfaces. *The Journal of Physical Chemistry C*, *112*(32), 12077–12080. <https://doi.org/10.1021/jp804078n>
- Dahm, T., Kruger, F., Stammler, K., Klinge, K., Kind, R., Wylegalla, K., & Grasso, J.-R. (2007). The 2004 Mw 4.4 Rotenburg, Northern Germany, earthquake and its possible relationship with gas recovery. *Bulletin of the Seismological Society of America*, *97*(3), 691–704. <https://doi.org/10.1785/0120050149>
- Dewers, T., & Hajash, A. (1995). Rate laws for water-assisted compaction and stress-induced water-rock interaction in sandstones. *Journal of Geophysical Research*, *100*(B7), 13093–13112. <https://doi.org/10.1029/95JB00912>
- Doornhof, D., Kristiansen, T. G., Nagel, N. B., Pattillo, P. D., & Sayers, C. (2006). Compaction and subsidence. *Oilfield Review*, *18*(3), 50–68.
- Dove, P. M. (1995). Geochemical controls on the kinetics of quartz fracture at subcritical tensile stresses. *Journal of Geophysical Research*, *100*(B11), 22349–22359. <https://doi.org/10.1029/95JB02155>
- Dove, P. M. (1999). The dissolution kinetics of quartz in aqueous mixed cation solutions. *Geochimica et Cosmochimica Acta*, *63*(22), 3715–3727. [https://doi.org/10.1016/S0016-7037\(99\)00218-5](https://doi.org/10.1016/S0016-7037(99)00218-5)
- Dove, P. M., & Crerar, D. A. (1990). Kinetics of quartz dissolution in electrolyte solutions using a hydrothermal mixed flow reactor. *Geochimica et Cosmochimica Acta*, *54*(4), 955–969. [https://doi.org/10.1016/0016-7037\(90\)90431-J](https://doi.org/10.1016/0016-7037(90)90431-J)
- Dove, P. M., & Elston, S. F. (1992). Dissolution kinetics of quartz in sodium chloride solutions: Analysis of existing data and a rate model for 25°C. *Geochimica et Cosmochimica Acta*, *56*(12), 4147–4156. [https://doi.org/10.1016/0016-7037\(92\)90257-J](https://doi.org/10.1016/0016-7037(92)90257-J)
- Dove, P. M., & Nix, C. J. (1997). The influence of the alkaline earth cations, magnesium, calcium, and barium on the dissolution kinetics of quartz. *Geochimica et Cosmochimica Acta*, *61*(16), 3329–3340. [https://doi.org/10.1016/S0016-7037\(97\)00217-2](https://doi.org/10.1016/S0016-7037(97)00217-2)
- Du, Q., Freysz, E., & Shen, Y. R. (1994). Vibrational spectra of water molecules at quartz/water interfaces. *Physical Review Letters*, *72*(2), 238–241. <https://doi.org/10.1103/PhysRevLett.72.238>
- Duan, Z., & Zhang, Z. (2006). Equation of state of the H₂O, CO₂, and H₂O–CO₂ systems up to 10 GPa and 2573.15K: Molecular dynamics simulations with ab initio potential surface. *Geochimica et Cosmochimica Acta*, *70*(9), 2311–2324. <https://doi.org/10.1016/j.gca.2006.02.009>
- Dunning, J. D., Douglas, B., Miller, M., & McDonald, S. (1994). The role of the chemical environment in frictional deformation: Stress corrosion cracking and comminution. *Pure and Applied Geophysics PAGEOPH*, *143*(1–3), 151–178. <https://doi.org/10.1007/BF00874327>
- Dunning, J. D., Petrovski, D., Schuyler, J., & Owens, A. (1984). The effects of aqueous chemical environments on crack propagation in quartz. *Journal of Geophysical Research*, *89*(B6), 4115–4123. <https://doi.org/10.1029/JB089iB06p04115>
- Ellsworth, W. L. (2013). Injection-induced earthquakes. *Science*, *341*(6142), 1225942. <https://doi.org/10.1126/science.1225942>
- Ferronato, M., Gambolati, G., Janna, C., & Teatini, P. (2010). Geomechanical issues of anthropogenic CO₂ sequestration in exploited gas fields. *Energy Conversion and Management*, *51*(10), 1918–1928. <https://doi.org/10.1016/j.enconman.2010.02.024>
- Finster, M., Clark, C., Schroeder, J., & Martino, L. (2015). Geothermal produced fluids: Characteristics, treatment technologies, and management options. *Renewable and Sustainable Energy Reviews*, *50*, 952–966. <https://doi.org/10.1016/j.rser.2015.05.059>
- Fisk, G. A., & Michalske, T. A. (1985). Laser-based and thermal studies of stress corrosion in vitreous silica. *Journal of Applied Physics*, *58*(7), 2736–2741. <https://doi.org/10.1063/1.335860>
- Frank, F. C., & Lawn, B. R. (1967). On the theory of Hertzian fracture. *Proceedings of the Royal Society of London. Series A: Mathematical and Physical Sciences*, *299*(1458), 291–306. <https://doi.org/10.1098/rspa.1967.0137>
- Gambolati, G., & Teatini, P. (2015). Geomechanics of subsurface water withdrawal and injection. *Water Resources Research*, *51*, 3922–3955. <https://doi.org/10.1002/2014WR016841>
- Gratier, J.-P., Guiguet, R., Renard, F., Jenatton, L., & Bernard, D. (2009). A pressure solution creep law for quartz from indentation experiments. *Journal of Geophysical Research*, *114*, B03403. <https://doi.org/10.1029/2008JB005652>
- Griffith, A. A. (1921). The phenomena of rupture and flow in solids. *Philosophical Transactions of the Royal Society of London, Series A, Containing Papers of a Mathematical or Physical Character*, *221*, 163–198.
- Hangx, S. J. T., Spiers, C. J., & Peach, C. J. (2010). Creep of simulated reservoir sands and coupled chemical-mechanical effects of CO₂ injection. *Journal of Geophysical Research*, *115*, B09205. <https://doi.org/10.1029/2009JB006939>
- Hanor, J. S. (1994). Origin of saline fluids in sedimentary basins. *Geological Society, London, Special Publications*, *78*(1), 151–174. <https://doi.org/10.1144/GSL.SP.1994.078.01.13>
- Heap, M. J., Baud, P., Meredith, P. G., Bell, A. F., & Main, I. G. (2009). Time-dependent brittle creep in Darley Dale sandstone. *Journal of Geophysical Research*, *114*, B07203. <https://doi.org/10.1029/2008JB006212>
- Hertz, H. (1882). Ueber die Berührung fester elastischer Körper. *Journal Für Die Reine Und Angewandte Mathematik*, *1882*(92), 156–171. <https://doi.org/10.1515/crll.1882.92.156>
- Hu, S., Li, X., & Bai, B. (2018). Effects of different fluids on microcrack propagation in sandstone under true triaxial loading conditions. *Greenhouse Gases: Science and Technology*, *8*(2), 349–365. <https://doi.org/10.1002/ghg.1744>

- Hu, S., Li, X., Bai, B., Shi, L., Liu, M., & Wu, H. (2017). A modified true triaxial apparatus for measuring mechanical properties of sandstone coupled with CO₂-H₂O biphasic fluid. *Greenhouse Gases: Science and Technology*, 7(1), 78–91. <https://doi.org/10.1002/ghg.1637>
- IEA. (2016). Tracking Clean Energy Progress 2016.
- Iler, R. (1973). Effect of adsorbed alumina on the solubility of amorphous silica in water. *Journal of Colloid and Interface Science*, 43(2), 399–408. [https://doi.org/10.1016/0021-9797\(73\)90386-X](https://doi.org/10.1016/0021-9797(73)90386-X)
- IPCC (2005). In B. Metz, O. Davidson, H. C. de Coninck, M. Loos, & L. A. Meyer (Eds.), *IPCC special report on carbon dioxide capture and storage*. Cambridge, United Kingdom and New York, USA: Cambridge University Press.
- Karner, S. L., Chester, F. M., Kronenberg, A. K., & Chester, J. S. (2003). Subcritical compaction and yielding of granular quartz sand. *Tectonophysics*, 377(3–4), 357–381. <https://doi.org/10.1016/j.tecto.2003.10.006>
- Knepper, T. (2003). Synthetic chelating agents and compounds exhibiting complexing properties in the aquatic environment. *Trends in Analytical Chemistry*, 22(10), 708–724. [https://doi.org/10.1016/S0165-9936\(03\)01008-2](https://doi.org/10.1016/S0165-9936(03)01008-2)
- Kosmulski, M. (2018). The pH dependent surface charging and points of zero charge. VII. Update. *Advances in Colloid and Interface Science*, 251, 115–138. <https://doi.org/10.1016/j.cis.2017.10.005>
- Kubicki, J. D., Sofo, J. O., Skelton, A. A., & Bandura, A. V. (2012). A new hypothesis for the dissolution mechanism of silicates. *The Journal of Physical Chemistry C*, 116(33), 17479–17491. <https://doi.org/10.1021/jp300623v>
- Lemmon, E. W., McLinden, M. O., & Friend, D. G. (2018). Thermophysical properties of fluid systems. In P. J. Linstrom, & W. G. Mallard (Eds.), *NIST Chemistry WebBook SRD 69*. Gaithersburg, Maryland: National Institute of Standards and Technology. <https://doi.org/10.18434/T4D303>
- Lindsay, C. G., White, G. S., Freiman, S. W., & Wong-Ng, W. (1994). Molecular orbital study of an environmentally enhanced crack growth process in silica. *Journal of the American Ceramic Society*, 77(8), 2179–2187. <https://doi.org/10.1111/j.1151-2916.1994.tb07115.x>
- Liteanu, E., Niemeijer, A. R., Spiers, C. J., Peach, C. J., & De Bresser, J. H. P. (2012). The effect of CO₂ on creep of wet calcite aggregates. *Journal of Geophysical Research*, 117, B03211. <https://doi.org/10.1029/2011JB008789>
- Menéndez, B., Zhu, W., & Wong, T.-F. (1996). Micromechanics of brittle faulting and cataclastic flow in Berea sandstone. *Journal of Structural Geology*, 18(1), 1–16. [https://doi.org/10.1016/0191-8141\(95\)00076-P](https://doi.org/10.1016/0191-8141(95)00076-P)
- Menin, A., Salomoni, V. A., Santagiuliana, R., Simoni, L., Gens, A., & Schrefler, B. A. (2008). A mechanism contributing to subsidence above gas reservoirs and its application to a case study. *International Journal for Computational Methods in Engineering Science and Mechanics*, 9(5), 270–287. <https://doi.org/10.1080/1550228080225234>
- Michalske, T. A., & Bunker, B. C. (1984). Slow fracture model based on strained silicate structures. *Journal of Applied Physics*, 56(10), 2686–2693. <https://doi.org/10.1063/1.333789>
- Michalske, T. A., & Freiman, S. W. (1982). A molecular interpretation of stress corrosion in silica. *Nature*, 295(5849), 511–512. <https://doi.org/10.1038/295511a0>
- Michalske, T. A., & Freiman, S. W. (1983). A molecular mechanism for stress corrosion in vitreous silica. *Journal of the American Ceramic Society*, 66(4), 284–288. <https://doi.org/10.1111/j.1151-2916.1983.tb15715.x>
- Moghadam, J. N., Mondol, N. H., Aagaard, P., & Hellevang, H. (2016). Experimental investigation of seismic velocity behavior of CO₂ saturated sandstones under varying temperature and pressure conditions. *Greenhouse Gases: Science and Technology*, 6(6), 734–751. <https://doi.org/10.1002/ghg.1603>
- Mossop, A. (2012). An explanation for anomalous time dependent subsidence. *46th US Rock Mechanics/Geomechanics Symposium 2012*, 1, 60–67.
- Nagel, N. B. (2001). Compaction and subsidence issues within the petroleum industry: From Wilmington to Ekofisk and beyond. *Physics and Chemistry of the Earth, Part A: Solid Earth and Geodesy*, 26(1–2), 3–14. [https://doi.org/10.1016/S1464-1895\(01\)00015-1](https://doi.org/10.1016/S1464-1895(01)00015-1)
- Nakata, Y., Hyodo, M., Hyde, A. F. L., Kato, Y., & Murata, H. (2001). Microscopic particle crushing of sand subjected to high pressure one-dimensional compression. *Soils and Foundations*, 41(1), 69–82. <https://doi.org/10.3208/sandf.41.69>
- NAM. (2015). Bodemdaling door Aardgaswinning—Nam-gasvelden in Groningen, Friesland en het noorden van Drenthe.
- Nangia, S., & Garrison, B. J. (2008). Reaction rates and dissolution mechanisms of quartz as a function of pH. *The Journal of Physical Chemistry A*, 112(10), 2027–2033. <https://doi.org/10.1021/jp076243v>
- Niemeijer, A. R., Spiers, C. J., & Bos, B. (2002). Compaction creep of quartz sand at 400–600°C: Experimental evidence for dissolution-controlled pressure solution. *Earth and Planetary Science Letters*, 195(3–4), 261–275. [https://doi.org/10.1016/S0012-821X\(01\)00593-3](https://doi.org/10.1016/S0012-821X(01)00593-3)
- Njiekak, G., Schmitt, D. R., Yam, H., & Kofman, R. S. (2013). CO₂ rock physics as part of the Weyburn-Midale geological storage project. *International Journal of Greenhouse Gas Control*, 16, S118–S133. <https://doi.org/10.1016/j.ijggc.2013.02.007>
- Ostermeier, R. M. (1995). Deepwater Gulf of Mexico turbidites—Compaction effects on porosity and permeability. *SPE Formation Evaluation*, 10(02), 79–85. <https://doi.org/10.2118/26468-PA>
- Parks, G. A. (1965). The isoelectric points of solid oxides, solid hydroxides, and aqueous hydroxo complex systems. *Chemical Reviews*, 65(2), 177–198. <https://doi.org/10.1021/cr60234a002>
- Parks, G. A. (1984). Surface and interfacial free energies of quartz. *Journal of Geophysical Research*, 89(B6), 3997–4008. <https://doi.org/10.1029/JB089iB06p03997>
- Pijenburg, R. P. J., Verberne, B. A., Hangx, S. J. T., & Spiers, C. J. (2018). Deformation behavior of sandstones from the seismogenic Groningen gas field: Role of inelastic versus elastic mechanisms. *Journal of Geophysical Research: Solid Earth*, 123, 5532–5558. <https://doi.org/10.1029/2018JB015673>
- Pijenburg, R. P. J., Verberne, B. A., Hangx, S. J. T., & Spiers, C. J. (2019). Inelastic deformation of the Slochteren sandstone: Stress-strain relations and implications for induced seismicity in the Groningen gas field. *Journal of Geophysical Research: Solid Earth*. <https://doi.org/10.1029/2019JB017366>
- Pluymakers, A. M. H., Peach, C. J., & Spiers, C. J. (2014). Diagenetic compaction experiments on simulated anhydrite fault gouge under static conditions. *Journal of Geophysical Research: Solid Earth*, 119, 4123–4148. <https://doi.org/10.1002/2014JB011073>
- Rijken, M. C. M. (2005). Modeling naturally fractures reservoirs: from experimental rock mechanics to flow simulation. University of Texas at Austin.
- Rohmer, J., Pluymakers, A., & Renard, F. (2016). Mechano-chemical interactions in sedimentary rocks in the context of CO₂ storage: Weak acid, weak effects? *Earth-Science Reviews*, 157, 86–110. <https://doi.org/10.1016/j.earscirev.2016.03.009>
- Samuelson, J., & Spiers, C. J. (2012). Fault friction and slip stability not affected by CO₂ storage: Evidence from short-term laboratory experiments on North Sea reservoir sandstones and caprocks. *International Journal of Greenhouse Gas Control*, 11, S78–S90. <https://doi.org/10.1016/j.ijggc.2012.09.018>
- Schimmel, M. T. W., Liu, W., & Worrell, E. (2019). Facilitating sustainable geo-resources exploitation: A review of environmental and geological risks of fluid injection into hydrocarbon reservoirs. *Earth-Science Reviews*. <https://doi.org/10.1016/j.earscirev.2019.03.006>

- Scholz, C. H. (1972). Static fatigue of quartz. *Journal of Geophysical Research*, 77(11), 2104–2114. <https://doi.org/10.1029/JB077i011p02104>
- Schutjens, P. M. T. M. (1991). Experimental compaction of quartz sand at low effective stress and temperature conditions. *Journal of the Geological Society*, 148(3), 527–539. <https://doi.org/10.1144/gsjgs.148.3.0527>
- Shalev, E., Lyakhovskiy, V., Ougier-Simonin, A., Hamiel, Y., & Zhu, W. (2014). Inelastic compaction, dilation and hysteresis of sandstones under hydrostatic conditions. *Geophysical Journal International*, 197(2), 920–925. <https://doi.org/10.1093/gji/ggu052>
- Silva, E. C. C. M., Li, J., Liao, D., Subramanian, S., Zhu, T., & Yip, S. (2006). Atomic scale chemo-mechanics of silica: Nano-rod deformation and water reaction. *Journal of Computer-Aided Materials Design*, 13(1–3), 135–159. <https://doi.org/10.1007/s10820-006-9008-y>
- Simpson, D. W., & Leith, W. (1985). The 1976 and 1984 Gazli, USSR, earthquakes—Were they induced? *Bulletin of the Seismological Society of America*, 75(5), 1465–1468.
- Spiers, C. J., De Meer, S., Niemeijer, A. R., & Zhang, X. (2004). Kinetics of rock deformation by pressure solution and the role of thin aqueous films. In S. Nakashima, C. J. Spiers, L. Mercury, P. A. Fenter, & M. F. J. Hochella (Eds.), *Physicochemistry of water in geological and biological systems*, (pp. 129–158). Tokyo: Universal Academy Press, Inc.
- Spiers, C. J., Hangx, S. J. T., & Niemeijer, A. R. (2017). New approaches in experimental research on rock and fault behaviour in the Groningen gas field. *Netherlands Journal of Geosciences*, 96(5), s55–s69. <https://doi.org/10.1017/njg.2017.32>
- Suckale, J. (2009). Induced seismicity in hydrocarbon fields. *Advances in Geophysics*, 51, 55–106. [https://doi.org/10.1016/S0065-2687\(09\)05107-3](https://doi.org/10.1016/S0065-2687(09)05107-3)
- Suckale, J. (2010). Moderate-to-large seismicity induced by hydrocarbon production. *The Leading Edge*, 29(3), 310–319. <https://doi.org/10.1190/1.3353728>
- Sverjensky, D. A., & Sahai, N. (1998). Theoretical prediction of single-site enthalpies of surface protonation for oxides and silicates in water. *Geochimica et Cosmochimica Acta*, 62(23–24), 3703–3716. [https://doi.org/10.1016/S0016-7037\(98\)00262-2](https://doi.org/10.1016/S0016-7037(98)00262-2)
- Takei, M., Kusakabe, O., & Hayashi, T. (2001). Time-dependent behavior of crushable materials in one-dimensional compression tests. *Soils and Foundations*, 41(1), 97–121. <https://doi.org/10.3208/sandf.41.97>
- Tamada, O., Gibbs, G. V., Boisen, M. B. Jr., & Rimstidt, J. D. (2012). Silica dissolution catalyzed by NaOH: Reaction kinetics and energy barriers simulated by quantum mechanical strategies. *Journal of Mineralogical and Petrological Sciences*, 107(2), 87–98. <https://doi.org/10.2465/jmps.110909>
- Tantayakom, V., Fogler, H. S., Charoensirithavorn, P., & Chavadej, S. (2005). Kinetic study of scale inhibitor precipitation in squeeze treatment. *Crystal Growth & Design*, 5(1), 329–335. <https://doi.org/10.1021/cg049874d>
- Tisato, N., Quintal, B., Chapman, S., Podladchikov, Y., & Burg, J. (2015). Bubbles attenuate elastic waves at seismic frequencies: First experimental evidence. *Geophysical Research Letters*, 42, 3880–3887. <https://doi.org/10.1002/2015GL063538>
- Van Eck, T., Goutbeek, F., Haak, H., & Dost, B. (2006). Seismic hazard due to small-magnitude, shallow-source, induced earthquakes in The Netherlands. *Engineering Geology*, 87(1–2), 105–121. <https://doi.org/10.1016/j.enggeo.2006.06.005>
- Van Eijs, R. M. H. E., Mulders, F. M. M., Nepveu, M., Kenter, C. J., & Scheffers, B. C. (2006). Correlation between hydrocarbon reservoir properties and induced seismicity in the Netherlands. *Engineering Geology*, 84(3–4), 99–111. <https://doi.org/10.1016/j.enggeo.2006.01.002>
- Van Thienen-Visser, K., & Breunese, J. N. (2015). Induced seismicity of the Groningen gas field: History and recent developments. *The Leading Edge*, 34(6), 664–671. <https://doi.org/10.1190/tle34060664.1>
- Wang, H. F. (2000). *Theory of linear poroelasticity with applications to geomechanics and hydrogeology*. New Jersey: Princeton University Press.
- Wiebes, E. (2018a). Gaswinning Groningen [Letter of government]. Retrieved March 29, 2018, from <https://www.rijksoverheid.nl/documenten/kamerstukken/2018/03/29/kamerbrief-over-gaswinning-groningen>
- Wiebes, E. (2018b). Gaswinning uit de kleine velden in de energietransitie [Letter of government]. Retrieved May 30, 2018, from <https://www.rijksoverheid.nl/documenten/kamerstukken/2018/05/30/kamerbrief-over-gaswinning-uit-kleine-velden>
- Wiederhorn, S. M. (1967). Influence of water vapor on crack propagation in soda-lime glass. *Journal of the American Ceramic Society*, 50(8), 407–414. <https://doi.org/10.1111/j.1151-2916.1967.tb15145.x>
- Wiederhorn, S. M., & Bolz, L. H. (1970). Stress corrosion and static fatigue of glass. *Journal of the American Ceramic Society*, 53(10), 543–548. <https://doi.org/10.1111/j.1151-2916.1970.tb15962.x>
- Wiederhorn, S. M., Freiman, S. W., Fuller, E. R., & Simmons, C. J. (1982). Effects of water and other dielectrics on crack growth. *Journal of Materials Science*, 17(12), 3460–3478. <https://doi.org/10.1007/BF00752191>
- Wiederhorn, S. M., Fuller, E. R., & Thomson, R. (1980). Micromechanisms of crack growth in ceramics and glasses in corrosive environments. *Metal Science*, 14(8–9), 450–458. <https://doi.org/10.1179/msc.1980.14.8-9.450>
- Wiederhorn, S. M., & Johnson, H. (1973). Effect of electrolyte pH on crack propagation in glass. *Journal of the American Ceramic Society*, 56(4), 192–197. <https://doi.org/10.1111/j.1151-2916.1973.tb12454.x>
- Wong, T. (1985). Geometric probability approach to the characterization and analysis of microcracking in rocks. *Mechanics of Materials*, 4(3–4), 261–276. [https://doi.org/10.1016/0167-6636\(85\)90023-7](https://doi.org/10.1016/0167-6636(85)90023-7)
- Xiao, Y., & Lasaga, A. C. (1994). Ab initio quantum mechanical studies of the kinetics and mechanisms of silicate dissolution: H⁺(H₃O⁺) catalysis. *Geochimica et Cosmochimica Acta*, 58(24), 5379–5400. [https://doi.org/10.1016/0016-7037\(94\)90237-2](https://doi.org/10.1016/0016-7037(94)90237-2)
- Xiao, Y., & Lasaga, A. C. (1996). Ab initio quantum mechanical studies of the kinetics and mechanisms of quartz dissolution: OH⁻ catalysis. *Geochimica et Cosmochimica Acta*, 60(13), 2283–2295. [https://doi.org/10.1016/0016-7037\(96\)00101-9](https://doi.org/10.1016/0016-7037(96)00101-9)
- Zdziennicka, A., Szymczyk, K., & Jańczuk, B. (2009). Correlation between surface free energy of quartz and its wettability by aqueous solutions of nonionic, anionic and cationic surfactants. *Journal of Colloid and Interface Science*, 340(2), 243–248. <https://doi.org/10.1016/j.jcis.2009.08.040>
- Zhang, J., Wong, T.-F., & Davis, D. M. (1990). Micromechanics of pressure-induced grain crushing in porous rocks. *Journal of Geophysical Research*, 95(B1), 341–352. <https://doi.org/10.1029/JB095iB01p00341>
- Zhang, S., & Liu, Y. (2014). Molecular-level mechanisms of quartz dissolution under neutral and alkaline conditions in the presence of electrolytes. *Geochemical Journal*, 48(2), 189–205. <https://doi.org/10.2343/geochemj.2.0298>
- Zhang, Y.-A., Tao, J., Chen, X., & Liu, B. (2014). Mixed-pattern cracking in silica during stress corrosion: A reactive molecular dynamics simulation. *Computational Materials Science*, 82, 237–243. <https://doi.org/10.1016/j.commatsci.2013.09.045>